

ABSTRACT

Title of Document: A MATHEMATICAL MODEL TO STUDY THE ROLE OF THE *LSR* INTERGENIC REGION IN MEDIATION OF AUTOINDUCER-2 QUORUM SENSING IN *ESCHERICHIA COLI*

Steven Meyer Graff, Master of Science, 2013

Directed By: Dr. William E. Bentley, Professor and Chair, Fischell Department of Bioengineering.

Quorum sensing (QS) is a process that allows bacteria to communicate with each other to coordinate collective behavior in response to changes in environmental conditions. Their ability to mediate biofilm formation of biofilms and antibiotic resistance has created challenges on healthcare systems, and an impetus for us to understand QS systems. QS mediated by autoinducer-2 is likely to be the most common of these mechanisms. Recent work has elaborated on the LuxS-regulated (Lsr) system which can mediate and process AI-2 to QS-dependent behaviors, particularly regulatory elements including the *lsr* intergenic region and the repressor LsrR, the so-called QS “switch”. In this thesis, we present a simulation of an example *lsr*-QS-system to elucidate the role of the *lsr* intergenic region binding site interactions and how this model integrates with recent literature on LsrR’s protein structure to provide further details on the mechanisms of how the switch may operate in real systems.

A MATHEMATICAL MODEL TO STUDY THE ROLE OF THE *LSR*
INTERGENIC REGION IN MEDIATION OF AUTOINDUCER-2 QUORUM
SENSING IN *ESCHERICHIA COLI*.

By

Steven Meyer Graff.

Thesis submitted to the Faculty of the Graduate School of the
University of Maryland, College Park, in partial fulfillment
of the requirements for the degree of
Master of Science
2013

Advisory Committee:
Professor William E. Bentley, Chair
Professor Hubert Montas
Professor Gregory Payne
Professor Ian White

© Copyright by
Steven Meyer Graff
2013

Dedication

To my family, but especially my loving parents Deborah and Gil, who have made great sacrifices for me so that I could pursue this work, and making me a better person. Without your love, your sacrifice, and your support, I would not be writing this work.

Acknowledgements

I would like to acknowledge the following people and organizations without which I would not have been able to pursue a master's. Thank you to the Bioengineering Graduate Program and the people involved with the program who allowed me to continue my graduate work after qualifiers.

I would like to thank the members of my Thesis Committee for their assistance throughout the Master of Science process. I would particularly like to acknowledge my advisor Dr. Bentley, who not only took me in when my former laboratory moved to the University of Houston, but also was a true mentor to me in every sense of the word.

I would like to acknowledge my peers in both the Bentley Lab now and my former peers in the Neural Engineering and Smart Prosthetics Lab for encouraging me with my work, helping me solve the many problems with my work, and navigate the world of laboratory and computational research.

Most importantly, I would like to thank the National Science Foundation and the Defense Threat Research Agency for providing me with the necessary funding for developing this model.

Table of Contents

Dedication.....	ii
Acknowledgements.....	iii
Table of Contents.....	iv
List of Figures.....	v
Chapter 1: Introduction.....	1
Chapter 2: Model Development.....	6
Section 1: Assumptions in the Model.....	7
Section 2: Detailed Development.....	9
Subsection 1: AI-2 Importation Module.....	10
Subsection 2: AI-2 Processing Module.....	14
Subsection 2.1: <i>l</i> srG-Dependent Degradation of Phospho-AI2.....	16
Subsection 3: Quorum Sensing Module.....	17
Subsection 3.1: LsrR Tetramer Cleavage.....	19
Subsection 3.2: <i>l</i> sr Expression and Output.....	21
Subsection 3.3: <i>l</i> sr Operon Repression.....	27
Subsection 4: cAMP-CRP Module.....	28
Subsection 5: Synthesis Module.....	30
Section 3: Model Implementation and Calibration.....	32
Subsection 1: Calibration of Transcription Constants k_{icR} and B	32
Subsection 2: General Model Implementation.....	35
Subsection 3: Implementation of Sensitivity Analysis.....	35
Chapter 3: Results.....	38
Section 1: Fitting the Basic Model Shows a Dynamic Response to the External AI-2 System.....	38
Section 2: Adjustments to the Model.....	49
Subsection 1: Effects of Specific Mutations.....	49
Subsection 1.1: The <i>l</i> srR Knockout (CB11 strain).....	50
Subsection 1.2: Reflecting Real Mutations in the Model.....	54
Chapter 4: Preliminary Conclusions.....	65
Chapter 5: Future Work.....	71
Section 1: cAMP-CRP Binding Interactions.....	71
Section 2: Promoter Binding Sequences.....	73
[Insert text here].....	Error! Bookmark not defined.
Section 3: Other modifications to the Model.....	80
Subsection 1: Incorporating AI-2 Importation and LsrK Dynamics.....	80
Subsection 2: Incorporating AI-2 Synthesis.....	81
Subsection 3: Incorporating Our Model Into a Population-Based Model.....	82
Subsection 4: Simulating the Effects of Inhibitors.....	83
Subsection 5: Algorithm Changes.....	85
Chapter 6: Supplemental Material.....	86
Section 1: Cooperative Binding Events.....	90
Section 2: Derivation of the Miller Unit-to-Concentration Conversion Factor, κ	93
References.....	108

List of Figures

Figure 1: Overview of our quorum sensing system	10
Figure 2: AI-2 importation pathway via the transporter Lsr.	11
Figure 3: AI-2 curve fitting	14
Figure 4: AI-2 processing module - steps involving lsrK and lsrG.....	16
Figure 5: Diagram of the quorum sensing module.....	18
Figure 6: The <i>lsr</i> operon containing the lsrR tetramer..	20
Figure 7: The cAMP-CRP module.....	29
Figure 8: Dynamics of <i>lsrK</i> -dependent phosphorylation reactions.	39
Figure 9: Tetramer cleavage reactions..	40
Figure 10: <i>lsr</i> operon de-repression and LsrR monomer synthesis.....	42
Figure 11: Production of <i>lsrR</i> transporter in the model.....	43
Figure 12: Beta-galactosidase activity associated with de-repression of the <i>lsr</i> operon.	44
Figure 13: Estimated values of k_{icR} and B.....	45
Figure 14: Re-formation of the tetramer..	47
Figure 15: Cyclic AMP regulatory dynamics.....	48
Figure 16: Wild type and <i>lsrR</i> knockout (CB11) fitted over time.....	50
Figure 17: <i>lsr</i> operon de-repression intermediates in wild-type (WT) and <i>lsrR</i> knockout (CB11) conditions	51
Figure 18: Wild type and <i>lsrR</i> knockout dynamics of LsrR and LsrACDB protein products.....	52
Figure 19: Bound dimer differentiation in wild type and <i>lsrR</i> knockout (CB11) conditions.....	53
Figure 20: Table of mutations studied in this thesis.....	55
Figure 21: Table of plasmids containing the mutations studied in this thesis.....	56
Figure 22: Table of results from simulations involving <i>lsrA</i> -directed mutants	58
Figure 23: Table of results from simulations involving <i>lsrR</i> -directed mutants	60
Figure 24: Binding and constants for each mutation experiment.....	61
Figure 25. General algorithm used for each mutagenesis experiment..	61
Figure 26: Representative shooting-based algorithm used to estimate $K_{bind lsrR}$ and $K_{bind lsrA}$ in mutation experiments.	62

Figure 27: Single strand genetic sequence (with mutations in complement) of the <i>lsr</i> intergenic region	66
Figure 28: Graphical representation of CRP binding site mutations.....	72
Figure 29: Simulation results of mutation experiments expressed in the <i>lsrA</i> direction.	72
Figure 30: Simulation results of mutation experiments expressed in the <i>lsrR</i> direction	72
Figure 31: Simulation results of promoter-site mutations in the <i>lsr</i> intergenic region in the <i>lsrA</i> direction.....	76
Figure 32: Simulation results of mutation experiments involving promoter-site mutations in the <i>lsrR</i> direction.	79
Supplementary Figure 1: Equations used in our model	86
Supplementary Figure 2: Parameters used in our conversion	96
Supplementary Figure 3: State variables in this model.....	97
Supplementary Figure 4: Constants used in this model. Error! Bookmark not defined.	

Chapter 1: Introduction

Bacterial biofilms have become a significant public health problem that have not only increased the cost of medical care by contaminating devices, but have been a significant means by which bacteria propagate antibiotic resistance. [1-4] The issue impacts many fields including implanted biomedical devices that become contaminated, such as prosthetic biomedical devices [1], include catheters[5-7], pacemakers[8,9], hip implants [1,10], and bone cement [11]. In urinary catheters alone, the development of urinary tract infections (UTIs) within catheters, and the resistance of bacteria to normal antibiotics have contributed to \$400 million (USD) in additional costs to utilize such devices alone, and have resulted in up to 1 million new cases of hospital transmitted infections annually[7]. There are several strategies that have been used to mitigate these infections. One strategy has been to simply swap the infected device with a replacement device. This presents a number of complications and increases the cost of those devices. Another strategy has been to treat the infections with antibiotics [7,12], or coat the devices with the antibiotic laden coatings or films [13-16]. While many trials have been performed, few had any impact on reducing infections owing to the complex dynamic of infection processes, particularly those that gain multiple antibiotic resistance. (We discuss some mechanisms of multiple antibiotic resistance later in this section.) Few trials have been carried out on complex biofilms containing multiple species of bacteria. Those that have reported some reduction in biofilm size, retain the possibility of increased antibiotic resistance or multiple antibiotic resistance in the surviving bacterial populations. In many cases of implanted devices, antibiotic resistance, even

with biocompatible materials, may still occur because the innate and adaptive immune systems may not recognize the surface as ‘self’, and thus not be ‘checked’ for pathogens because the ‘sensing’ neutrophils and lymphocytes may not be able to access the surface [17] (as one mechanism for assessing what is considered “self” vs “non-self” or “foreign”).

Antibiotic resistance does not just happen in cases of implantable biomedical devices, but has been occurring in increasing frequencies independent of those from implantable devices. For instance, in some hospital tests for *E. coli* infections, over 90% of the bacteria identified were multi-drug resistant [18,19]. The increasing frequency of vancomycin-resistant *Enterococci* (VRE)[20-28], and multiple drug resistant (MDR) *Staphylococcus aureus* (MRSA)[29-38] infections raises the concern that much of the current stock of antibiotics may be rendered useless against common infections. (In most cases, vancomycin is regarded as the ‘antibiotic of last resort’, due its strength and side effects [39].) In these bacteria, antibiotic resistance can be mediated through physical barriers that either keep bacteria without means to resist or utilize the antibiotic in a positive manner[4,40], or without efflux pumps to physically pump out the antibiotic once the antibiotic is recognized [2,41,42]. These efflux pumps and biofilm behaviors are described in great detail elsewhere.

Nevertheless, the organization within those biofilms, and the ability of bacteria in biofilms to survive antibiotic treatment suggest that if bacterial colonies can be localized such that they remain planktonic (not form a biofilm), there would be many possibilities for improvement towards solutions that can not only prevent antibiotic resistant device contamination, but also improve the efficacy of antibiotics

in treating infections. For that to happen, there needs to be some sort of central linking behavior that may cause bacterial colonies in one condition to remain planktonic, and for bacteria to form biofilms in another. This link can be based on nutrient availability, tensile or shear stress in the system, or on other stresses. Most importantly, this link is based on number density—how many bacterial cells are in a given area at a certain time. When bacteria would perceive this number density to be higher than a threshold exists, or a “quorum”—meaning that there may be too many members in an area to share resources and remain planktonic— so they may form a biofilm, or become virulent, or otherwise coordinate their behavior as a collective unit, taking on phenotypes that aid in determining their fate. Examples of collective behaviors that are regulated by quorum sensing are the establishment of biofilms, the attachment of pathogenic *E. coli* to epithelial cells, the transference of virulence factors, etc. Excellent reviews have appeared that explain the mechanisms of the signal transduction processes as well as additional examples of the emergent behaviors [43-52] [53] (UK). Briefly, these bacteria synthesize molecules dedicated to quorum sensing (**quorum sensing molecules**). When the concentration of these molecules is above threshold, and depending on external conditions, the quorum sensing molecule can be imported, processed, and induce the expression of genes that contribute to the formation of a biofilm, to virulence, to other behaviors including the facilitation of chemotaxis[54].

Quorum sensing (QS) molecules can be classified into three different categories—N-acylhomoserine lactones (AHLs) including autoinducer-1s (AI-1s) that mediate intraspecies signaling, autoinducers such as autoinducer-2 (AI-2) and

autoinducer-3 (AI-3) that may mediate both interspecies and intraspecies quorum sensing. Of these, AI-2 is the most ubiquitous, and most utilized of the known QS molecules[55]. Because of its detection among many species, and because many species contain a conserved pathway which produces AI-2 (which will be described in later sections), AI-2 producing and sensing systems have drawn significant interest.

Based on their availability, and their application to a common class of MDR infections, we utilize the *Escherichia coli* (*E. coli*) QS system, and in particular, the *E. coli* K12 LuxS-regulated (Lsr) quorum sensing system as our system of interest.

The current understanding of this circuit was described in Hooshangi and Bentley, and Tsao et al [56-58], and will be explained in more detail in later sections.

Recently, however, our laboratory has undertaken a systematic study of the mechanisms of the transcriptional control circuits for this system. Byrd has developed new insight on the effects of the lone repressor in this system, LsrR, on gene expression in the bicistronic *lsr* regulon[59]. Influencing the interactions between LsrR and the *lsr* regulon have become a major starting point for the development of QS inhibitors, although initial studies have only targeted the prevention of the derepression of the *lsr* regulon [44,60,61], or efflux pumps that may pump out antibiotics. [62] Importantly Byrd demonstrated through genetic mutation of the intergenic region within the *lsr* regulon (between *lsrRK* and *lsrA*) that there are putative binding sites for CRP and LsrR that when considered in more detail reveal the possible existence of dimer and tetrameric forms of LsrR that play a role in the transcription of the *lsr* regulon.

This thesis builds on the concepts of Hooshangi and Bentley [43] , but adds significantly more complexity to the regulatory cascade; the desire being to strike a mathematical representation of the results of Byrd. The thesis is organized into component parts: a section on Model Development; a section on Simulation Results; a section on Concluding Remarks; and finally, a section on Future Work that might reveal additional insight beyond the factors considered here.

Chapter 2: Model Development

Previous work by Hooshangi and Bentley [43] demonstrated that we could build a simple deterministic model of the *lsr* AI-2 quorum sensing regulatory network, based on knockout experiments of regulatory components. However, more recent studies have revealed more mechanistic detail of the transcriptional regulation and secondary regulators to the quorum sensing response. Therefore, we have reevaluated Hooshangi and Bentley's model and significantly modified the model to improve its relevancy to a more sophisticated model experimental system.

In order to develop our model, we needed to make some basic assumptions. These assumptions are elucidated in Section 1.

Section 1: Assumptions in the Model

Assumption 0: We have developed an idealized time-dependent profile for the appearance and disappearance of AI-2 that follows typical batch experiments of wild-type *E. coli* K12 strains[63,64]. We consider this profile as a fixed profile that the model dynamics will be built around.

Assumption 1: The model cell contains a mutation in the gene sequence of *lsrB*, meaning the transporter Lsr can be inserted into the plasma membrane of our model *E. coli* cell, but it cannot import AI-2. Likewise, this cell contains the Δpts mutation, which knocks out the PTS pathway that is considered to be an alternate pathway for AI-2 importation besides the one through Lsr[65-67], and *lsrK* (Lsr transporter). Therefore, all phosphorylation of AI-2 occurs via the pathway through LsrK, and all AI-2 is imported into our cell by simple diffusion. With simple diffusion governing the AI-2 import, intracellular AI-2 that has not been converted to phospho-AI2 (AI2-P) is assumed to reach rapid equilibrium with extracellular AI-2 concentration. This equilibrium between intracellular and extracellular AI-2 exists at all times throughout our simulation.

Assumption 2: Lsr kinase (from *lsrK*), the enzyme which phosphorylates AI-2 when imported through either the main pathway or through simple diffusion, is permanently stable. We allow our cell to express *lsrK* normally prior to all our simulations, and knock out *lsrK* before the start of any simulation. Therefore, we assume that no lsrK is made, and that lsrK's activity can be represented by a single maximum rate constant, k_{lsrK} .

Assumption 3: The amount of ATP consumed by our system is negligible to that which is consumed by other cellular processes. Therefore, we assume ATP concentrations inside the cell remain constant throughout all simulations.

Section 2: Detailed Development

For simplification, our model of the *lsr* quorum sensing in *LuxS* knockouts is divided into four modules, which are summarized by Figure 1. Briefly, AI-2 is imported into our model cell via the **AI-2 Importation Module** (if not through the so-called alternative pathway involving the phosphoenolpyruvate (PEP) transferase system) and processed via **AI-2 Binding/Processing Module**, which produces AI2-P. This AI2-P triggers derepression of **Quorum Sensing (QS) Response Module**, which produces a number of outputs including activation of the **AI-2 Importation Module** and the **AI-2 Binding/Processing Module**, or repression of the **Quorum Sensing Response Module**. This **Quorum Sensing Response Module** is regulated by input from the **cAMP/CRP Module**. These modules will be described in the next several sections, which include our descriptions of the equations that describe the activities going on in each of these modules.

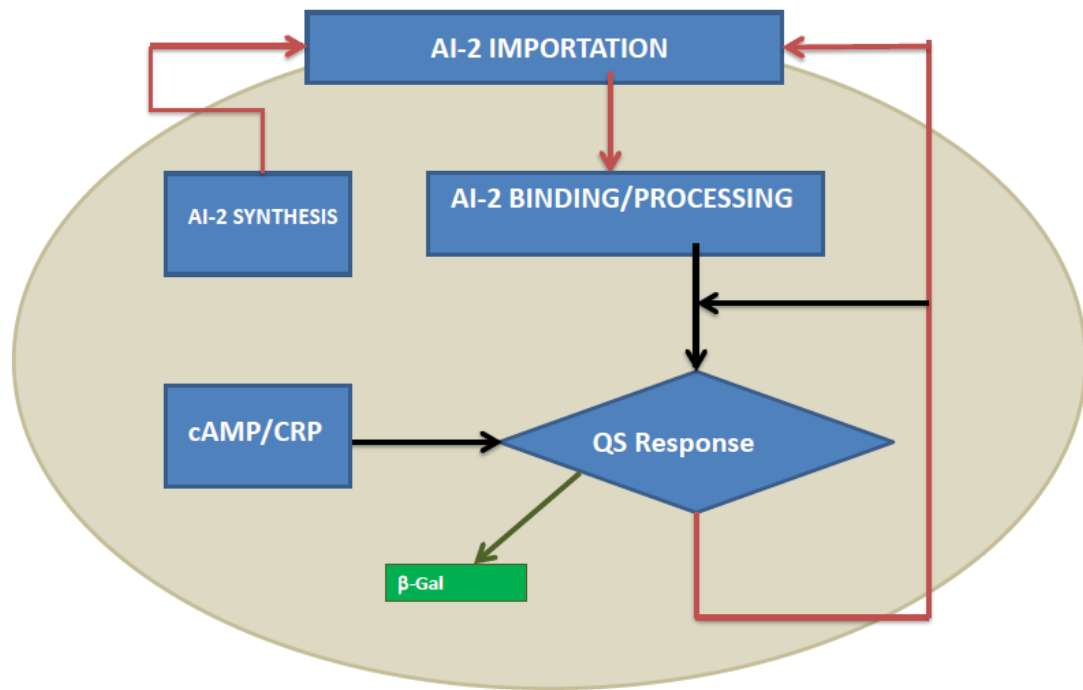


Figure 1: Overview of our quorum sensing system as divided into its basic components. Arrows govern the flow of outputs to inputs. Arrowheads pointing into an icon represent inputs, while arrows pointing away from our module in question represent outputs of our system. Connections in red represent conditions, and output flow that is not included in our model. The assumptions we make in Section 1, as well as throughout this discussion, are implemented instead.

Subsection 1: AI-2 Importation Module

In order for AI-2 to have any influence inside the *E. coli* cell, it must be imported into the cell. Importation into bacterial cells can happen through either simple diffusion or through some receptor-mediated process. Evidence has been built up for the existence of two different AI-2 internalization pathways in Enteric bacteria. The first is through a receptor-mediated process mediated by Lsr, the transporter that is produced by the *lsrACDB* flank of the *lsr* operon. Lsr is a multimeric membrane protein complex with two membrane-bound domains (*lsrA* and *lsrC*) and two active domains (*lsrB* and

l_{srD}). Crystallographic studies have suggested that Lsr functions similar to an ATP-binding cassette protein [46], requiring ATP phosphorylation and dephosphorylation in order to shuttle AI-2 into the cell and recycle Lsr. This process is diagrammed in detail in Figure 2. Briefly, if environmental AI-2 is above a threshold concentration, it will initially bind to the LsrB domain of Lsr. Upon the phosphorylation of Lsr's intracellular domains via ATP, Lsr undergoes a change in conformation, and shuttles and releases AI-2 inside the cell. Once AI-2 is inside the cell, Lsr is dephosphorylated and returns to the original state, to import more AI-2. Through the production of Lsr, induction of the *lsr* operon (which we define as the Quorum Sensing Module), affects the rate at which AI-2 imported through Lsr.

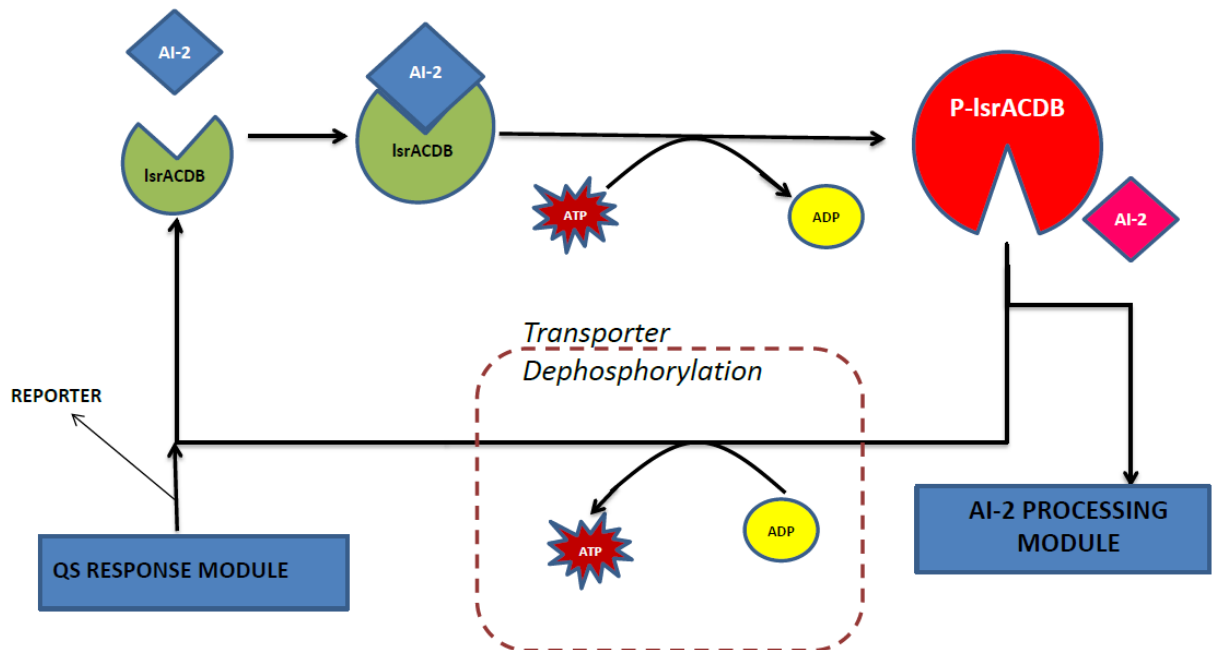


Figure 2: AI-2 importation pathway via the transporter Lsr.

While Lsr was the first transporter identified, Pereira and colleagues (cite) suggested that knocking out *lsrACDB* (*lsrA* + *lsrC* + *lsrD* + *lsrB*), the genes that

produce Lsr, did not significantly reduce AI-2 internalization. While *lsrACDB* was considered to be a main transporter system, another transport system, knocking out the phosphoenolpyruvate transferase system (PTS), produced a much more significant drop in AI-2 internalization [66,67]. However, how exactly PTS interplays within Lsr-independent AI-2 import remains unclear, and does whether PTS is the main component through which initial AI-2 import. Until we know further details, we will assume a time-dependent profile of AI-2 which is observed outside the cell and is exactly mimicked by the intracellular domain. In essence, while we know it is not the case, our assumption is akin to rapid equilibrium of AI-2 and AI-2P outside and inside the cell membrane. It is this profile that initiates the quorum sensing regulatory structures at predetermined times. We can also force AI-2 importation (via Lsr) to happen via making a point mutation in *lsrA* and *lsrC* that renders Lsr unable to bind to the plasma membrane.

In wild-type *E. coli* cells containing LuxS, once the LuxS produces the AI-2 precursor (DPD) and this is converted to AI-2, it has been proposed that this AI-2 leaves the cell through interactions with a secondary transporter protein known as YdgG (or TqsA) [68]. It remains unclear however, how YdgG operates to export AI-2, or if YdgG is even significant for AI-2 export in *E. coli*. So, for simplicity, we assume that this process happens through simple and rapid diffusion; and we can effectively ‘knock out’ the gene producing YdgG, *ydgG*, or otherwise disregard its activity. Our discussion of YdgG will be described in more detail in the synthesis section.

Because we have now assumed AI-2 diffusion can happen both in the forward and reverse direction, we now assume that there is an equilibrium state between intracellular and extracellular AI-2. Assuming this happens rapidly, Assumption 1 holds true for our cell. Therefore, we will assume import always happens, and PTS acts as a secondary regulator that is always on.

While our model cell is incapable of producing or exporting AI-2, we must acknowledge our cells can still be placed into a dynamic AI-2 environment. Luo and colleagues demonstrated such a real system could be set up [69]. So, we set up a virtual machine controlling AI-2 concentration in our virtual batch, such that we see how our system responds as extracellular (and intracellular) concentrations of AI-2 increase to some peak and then decrease to near zero levels.

To do this, we fitted a pseudo-Gaussian curve to AI-2 activity data observed by Liang Wang et al [63,64], with the small conversion, which we assume here as $1\mu\text{M AI-2} = 1600$ activity units BB170, and parameters α , β , and γ , parameters that define the characteristics of our pseudo-Gaussian function. (We call it a pseudo-Gaussian curve because we are not dealing with probability distributions. True Gaussian functions, as we define them, represent probability distributions whose areas under the curve must equal 1 by definition.) The values from our fit are listed in Table 1, and the fit when compared to Liang Wang's data is shown in Figure 3. This continuous function can be differentiated over time and used directly as a dynamic model input that is later integrated simultaneously with all other state variables.

$$A_a(t) = \alpha e^{-\left(\frac{t-\beta}{\gamma}\right)^2} \quad (1)$$

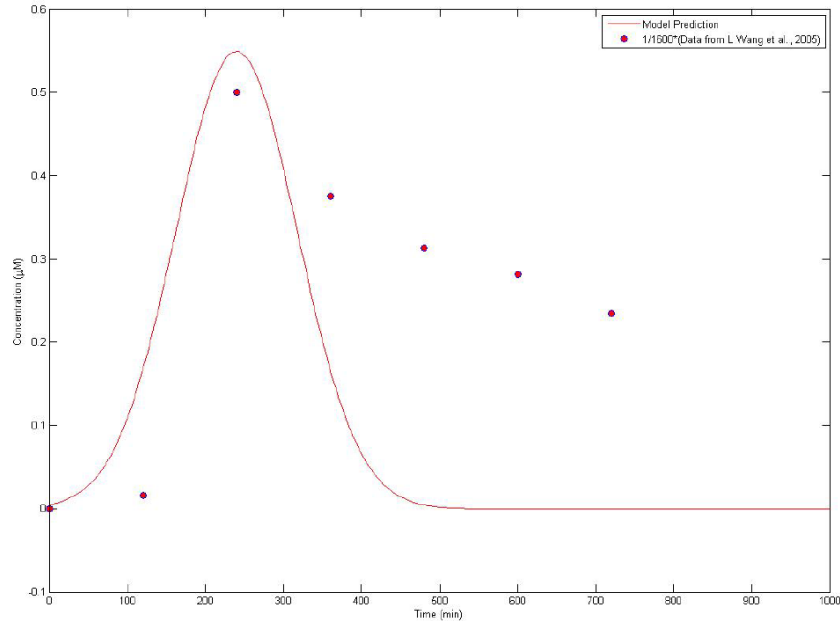


Figure 3: AI-2 Curve Fitting AI-2 curve (solid red line) fitted to data from [63] with the conversion factor of 1600 AI-2 activity units/1 uM AI-2 (blue filled circles)

That is, we can now differentiate our form for $A_o(t)$, our autoinducer-2 concentration profile, yielding a variable input into our *lsr* system to obtain our ODE equation for our autoinducer-2 concentration in (2) (or I in Supplementary Figure 1).

$$\frac{dA_o}{dt} = -2 \left(\frac{\alpha(t-\beta)}{\gamma} \right) e^{-\left(\frac{t-\beta}{\gamma}\right)^2} \quad (2)$$

Subsection 2: AI-2 Processing Module

While many studies have correlated AI-2 to the expression of the *lsr* operon, and other *lsr*-dependent genes, we also know that AI-2 (in whatever form is recognized by the species of bacteria in question) cannot directly activate transcription of *Lsr*[70,71]. Genetic structural analysis of a gene downstream from *lsrR* by Taga et al. identified a new gene in *S. typhimurium* that was homologous to

bacterial carbohydrate kinases—indicating that the new gene was likely a phosphatase. Because of its location within the operon, the new gene was dubbed *lsrK*, which produced the protein LsrK (luxS-regulated kinase). Further experiments by Wang et al., 2005; Hooshangi and Bentley, Taga et al, and others which studied the effects of knocking out this new gene on transcription of the *lsr* operon [43,46,63,71] in *E. coli* and *S. typhimurium* suggested a strong correlation between knocking out *lsrK* and strongly reduced expression of Lsr, implying that LsrK converts AI-2 into an active form in order to de-repress the *lsr* operon. Taga et al, also performed ATPase assays on the new protein *in vivo* and demonstrated that LsrK had ATPase activity, and therefore LsrK was actually a kinase.

A summary of our “AI-2 processing” module, as initially presented in this section, is diagrammed in Figure 3. Briefly, AI-2 that has been internalized into the cell binds to LsrK, and LsrK transfers a phosphate group from ATP (which also binds to LsrK) to AI-2, converting AI-2 to the active phosphorylated form, AI-2-P. Upon the release of AI-2-P, LsrK can take on another molecule of AI-2, and AI-2-P can follow on one of two paths---1) it can be simply degraded through a *lsrG*-dependent pathway initially identified by Marques and colleagues [72] , or 2) it can activate the ‘quorum sensing response’, which will be detailed by the Quorum Sensing Module.

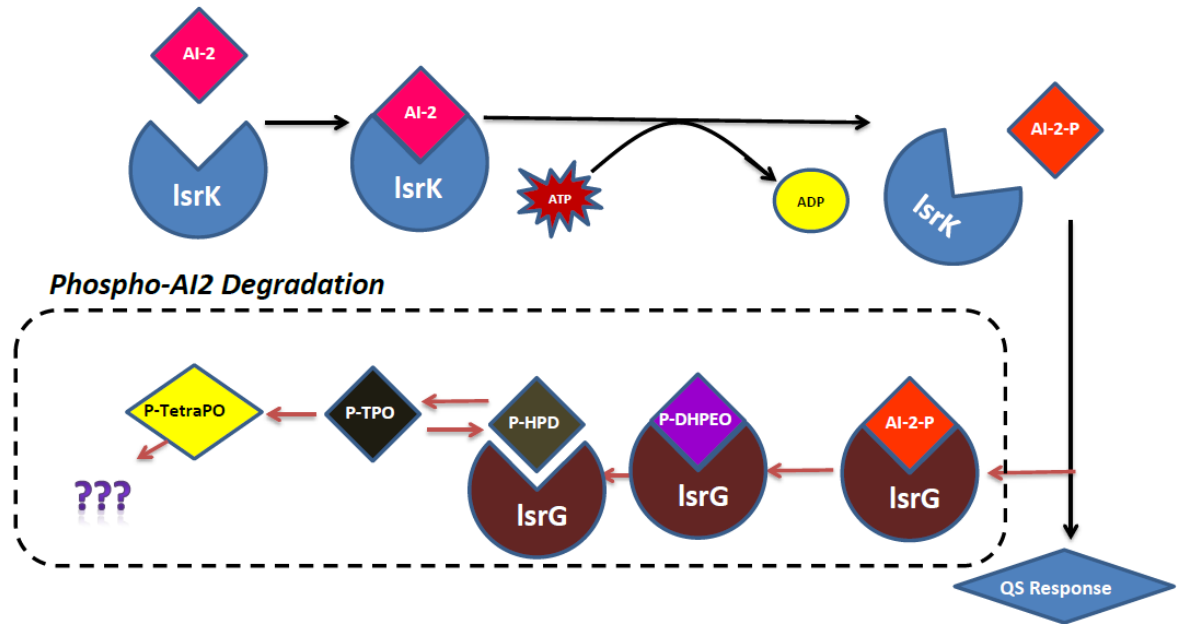


Figure 4: AI-2 processing module - steps involving *lsrK* and *lsrG*.

Ordinary differential equations (ODEs) detailing components of the AI-2 processing module were derived from Figure 3, following the arrows in black (in general terms). These ODEs, including our ATP equation based in Assumptions 2 and 3, are detailed in equations II-IV in Supplementary Figure 1.

Subsection 2.1: *lsrG*-Dependent Degradation of Phospho-AI2

While *lsrG* had been identified as one of the genes expressed when AI-2 derepresses the *lsr* operon, its function had not been clearly identified until recently. In 2007, Xavier and colleagues demonstrated that *LsrG* could convert AI-2-P to two polyglycolic acids. However, they observe that one polyglycolic acid (PGA) appears in larger amounts *in vitro* than does the other acid, suggesting that one PGA could be converted into another. So, Marques et al. created Δ *lsrG* *E. coli* mutants and tested the effects of knocking out *lsrG* on *Lsr* expression, as determined by inserting a β -

galactosidase reporter gene downstream from *lsrACDB* [72]. In the Δ lsrG strains, they find, through NMR studies, that AI-2-P accumulates intracellularly in levels close to tenfold higher than in cells containing *lsrG*. They also identified the two different PGAs that appeared in Xavier et al.'s 2007 study [70] as 3-hydroxy-2,4-pentadione-5-phosphate (P-HPD) and 3,3,4-trihydroxy-2-pentanone-5-phosphate (P-TPO) [72], an intermediate between AI-2-P and P-HPD known as 3,4-dihydropent-3-en-2-ol-5-phosphate (P-DHPEO), and a final product from the non-enzymatic oxidation of P-TPO, which is 3,3,4,4-tetrahydroxy-2-pentanone-5-phosphate (P-TetraPO). It is still unclear what happens with P-TetraPO [72], and so for modeling purposes, we simply assume that the modeling pathway is a degradation pathway that can be summarized by a single degradation rate constant k_{deg_Ap} , which is defined in Supplementary Figure 3.

Subsection 3: Quorum Sensing Module

Once LsrK phosphorylates imported AI-2 to form AI-2-P, it enters into our Quorum Sensing Module, , which can be summarized by Figure 4 and divided into several steps that include 1) cleavage of the LsrR tetramer, 2) the subsequent expression of the *lsr* operon and 2) the reformation of the LsrR tetramer.

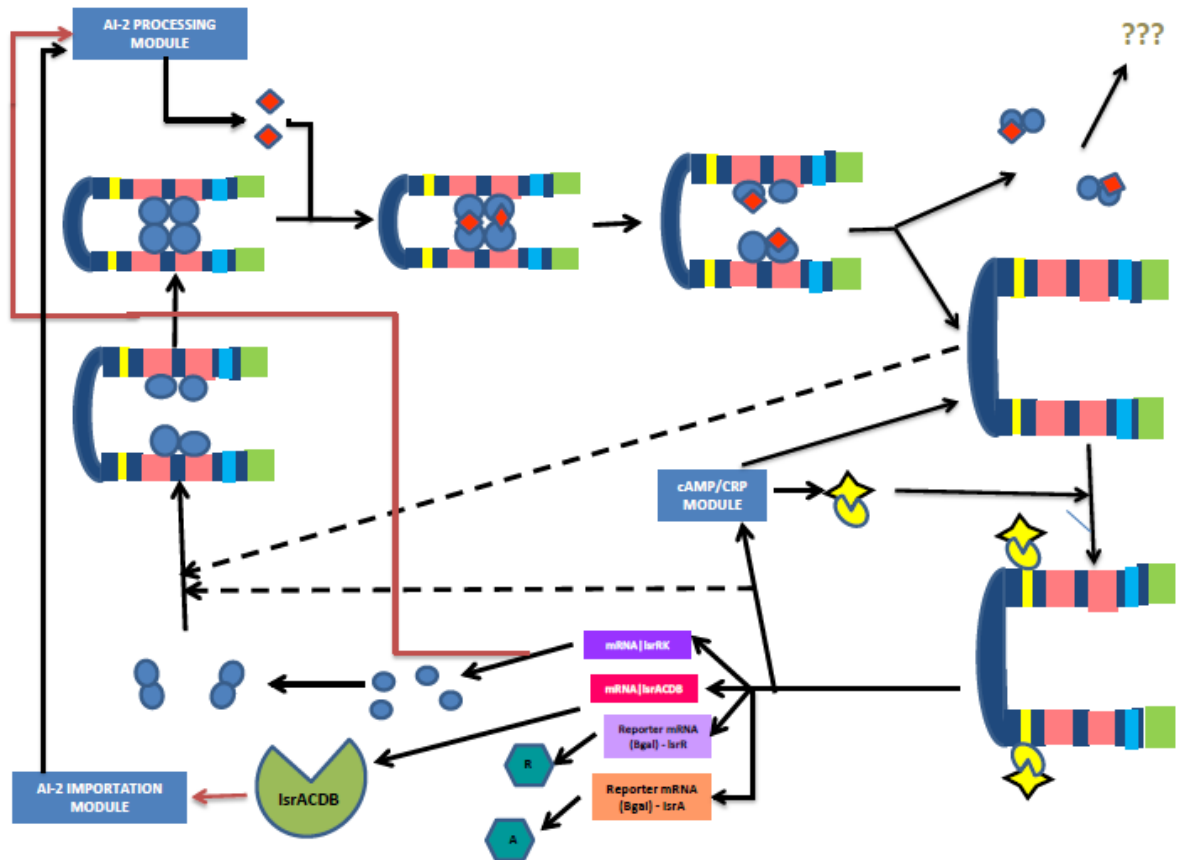


Figure 5: Diagram of the quorum sensing module. Binding of AI-2-P (red diamonds) to the LsrR tetramer (blue circles, bound to binding sites marked by a salmon-color) lead to the splitting apart of the tetramer into two dimers and the eventual cleavage of the AI-2-P LsrR dimers off of the *lsr* operon, partially derepressing the *lsr* operon. Binding of cAMP-CRP (yellow star with yellow 'pac-man') to the CRP-binding sites (yellow on *lsr* operon) as a result of events in the cAMP-CRP module result in the full activation of transcription of the *lsr* operon, which produces mRNA for genes on both flanks of the *lsr* operon, as well as mRNA for the reporter (*lacZ*) associated with either *lsrRK* or *lsrACDB*. The mRNA is then translated into *lsrR* monomer (blue circles), Lsr (green pac-man), and beta-galactosidase (teal hexagons). If LsrK is functional, expression of *lsrK* would feed back to the AI-2 processing module (red arrow). If LsrACDB is function, expression of *lsr* would facilitate more importation of AI-2. LsrR dimerizes to form the free dimer (two circles), then binds to its binding sites on the *lsr* operon. The two bound dimers are then brought together to reform the LsrR tetramer.

Subsection 3.1: LsrR Tetramer Cleavage

The first step of the quorum sensing process involves the binding of AI-2-P (phospho-AI2) to LsrR. Experimental studies suggested that, based on genetic homology to similar proteins and preliminary crystallography studies [73], that LsrR exists as a tetramer when bound to four ‘operator’ (O) binding sites (putative binding half-sites) identify by Byrd as shown in Figure 6. We propose that the cleavage occurs as a two-step process. First, two AI-2-P molecules bind to the tetramer, cleaving the tetramer into two LsrR dimer-AI-2-P complexes still bound to their binding sites. Then, due to the instability of the LsrR dimer-AI-2-P-DNA complexes, the LsrR dimer-AI-2-P complexes are subsequently released from the putative binding half-sites.

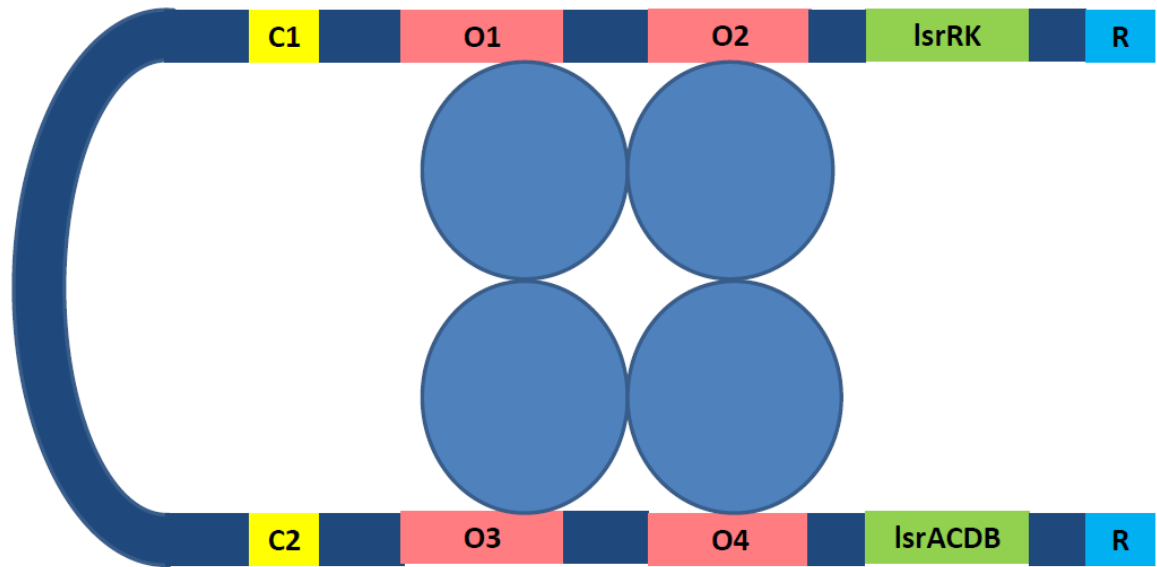


Figure 6: The *lsr* operon containing the *lsrR* tetramer. (The LsrR tetramer consists of the blue circles bound joined together). The *lsrR* tetramer is bound to the operon at binding sites O1, O2, O3, and O4 (salmon rectangles). Removal of *lsrR* triggers the expression of *lsrACDB* (bottom, in green) or *lsrRK* (top, in green), and their associated reporters (signified by R, in light blue). cAMP-CRP complexes can enhance and fully activate expression of the *lsr* operon by binding to CRP-binding sites C1 and C2 (yellow).

These steps occur given a few premises. First, we assume that since the tetramer itself is formed by the binding of two homodimers, there have to be two binding sites on the homodimers (one on each homodimer) required to break apart the tetramer into two LsrR dimer-AI-2-P complexes removed from the *lsr* operon or else, we assume, we may still see complete repression of either flank of the *lsr* operon. The particular flank that would still be repressed would be the flank whose dimer is not bound to AI-2-P. We also assume that changes in the intermolecular forces, whether hydrophobic, steric, or electrostatic, between the dimer-AI-2-P complexes and their associated DNA molecules are strong enough to forces the complexes off of their associated binding sites, and that these complexes are degraded by an unknown

pathway in which neither LsrR dimer nor AI-2-P are recycled back into the regulatory circuit.

Given these assumptions, we now identify our governing rate constants and state variables that are used in our model. The initial binding reaction of AI-2-P with the tetramer that forms the LsrR dimer-AI-2-P complexes bound to the *lsr* operon are governed by the rate constant k_{bind} (see Supplementary Figure 4), and the cleavage reactions of the dimer-AI-2-phosphate complexes off of the associated dimer binding sites are governed by k_{cleave1} (*lsrRK*) and k_{cleave2} (*lsrACDB*). Bulk (LsrR) tetramer, AI-2-P, (LsrR) dimer/*lsrRK* complex, dimer/AI-2-P/*lsrACDB* complex, dimer/AI-2-P complex, free *lsrRK* and free *lsrACDB* concentrations are represented by the state variables (listed in Supplementary Figure 3) T_b , A_p (from the AI-2 Processing Module), $D_{p_b|lsrR}$, $D_{p_b|lsrA}$, D_p , *lsrR*, and *lsrA* respectively.

Subsection 3.2: *lsr* Expression and Output

Once LsrR has been released from its binding sites near *lsrRK* (Δ *lsrK*) and *lsrACDB*, one would presume that expression of *lsrR* is straight forward—*lsrACDB*, *lsrR* and their associated reporters are transcribed (mRNA encoding each is produced), and translated into proteins (and an output for the β -galactosidase activity assay) including the monomer form of *lsrR*, and the transporter. We initially assume the transcription equations have the form shown in equation 18, for only the *lsrACDB* flank (transcribing monomer), where *lsrA* is previously defined. We introduce a constant, B , that represents the observed bias towards *lsrR* with the conditions held in 19. Maximum rate constant, k_{tcR} is the basal transcription rate for *lsrR*, $k_{\text{deg_mRNA}}$ is the mRNA-specific degradation rate. We will initially assume k_{tcR} and $k_{\text{deg_mRNA}}$ for

our system are known and that *lsr* expression is not biased to either flank, for the purposes of our discussion.

$$\frac{d(mRNA|lsrA)}{dt} = Bk_{tcR}(lsrA) - k_{deg_mRNA}(mRNA|lsrA) \quad (18)$$

$$B : \begin{cases} B > 1 & \text{Biased expression towards } lsrACDB \\ B < 1 & \text{Biased expression towards } lsrRK \\ B = 1 & \text{lsr expression is unbiased} \end{cases} \quad (19)$$

However, establishing unregulated transcription and translation after an initial activation event is a dangerous concept in modeling of biological systems. Several studies have suggested that cyclic-AMP (cAMP) acts as such a regulator through interactions with its receptor protein (cAMP receptor protein, or CRP)[74,75], which can, in turn, positively regulate expression of a target gene by improving the access of RNA polymerases and transcription regulatory proteins to the target sequence. In our particular case, cAMP-CRP binding to a DNA region upstream of either flank of the *lsr* operon could positively regulate expression of the *lsr* operon. While the DNA binding sections were identified as being upstream of *lsrACDB* and *lsrRK*, little was known about the role of the binding site sequences themselves because studies examining the role of cAMP-CRP binding in *lsr* regulation only addressed the role of the production of CRP. Then, Wang et al., positively demonstrated the binding of CRP to the operator regions within the intergenic *lsr* regulatory region [64]. Sequencing work by Byrd [59,76] identified the exact sequences for the two CRP binding sites in the *lsr* operon, labeled as C1 and C2 in Figure 5. This work also allowed him to directly introduce mutations into either CRP binding site (or both), and identify the role that the binding site sequence could play in mediating the regulation of the expression of *lsr*. When a point mutation was introduced at either site C1 (near *lsrRK*), or C2 (near *lsrACDB*), expression of either *lsrRK* or *lsrACDB*

(as measured by the β -galactosidase activity associated with a reporter *lacZ* attached immediately downstream of either *lsrRK* or *lsrACDB*) is reduced by 96% from the wild type population (*E. coli* containing intergenic plasmids containing unmutated C1 and C2 sections), which provided an effect that was slightly stronger than was knocking out CRP. Therefore, we must take into account the ability of CRP, in particular cAMP-CRP complexes to bind to its binding site, as an effector of *lsr* mRNA synthesis. (We will detail the modeling of this particular process in section B.4, when we discuss the cAMP module.)

The positive regulation we see with cAMP-CRP on transcription of the *lsr* operon is similar to those that have been modeled for β -galactosidase production in low-glucose conditions [75], as shown in equation 20. We will call this modifier Ω , and define it in terms of cAMP:CRP:C2 (cAMP-CRP complexes bound to site C2) and C2 (free C2 sites), and incorporate it as a multiplier before 18 to our next form of transcription as shown in equation 22. Increasing Ω increases the transcription rate of our transporter (and associated reporter). We will test our assumption of this form of Ω against the form of Ω , which we call Ω^* in (21) which is part of the modifications we make to our model to determine whether our assumption will hold, later in this study when we modify the base model.

$$\Omega = \frac{cAMP:CRP:C2}{C2} \quad (20)$$

$$\Omega^* = \frac{cAMP:CRP:C2}{C2 + cAMP:CRP:C2} \quad (21)$$

$$\frac{d(mRNA|lsrA)}{dt} = Bk_{tcR} \left(\frac{cAMP:CRP:C2}{C2} \right) lsrA - k_{degmRNA} (mRNA|lsrA) \quad (22)$$

We must now consider the possibility of transcriptional bias in our system. Transcriptional bias can arise in a biological system when a derepression event induces expression of genes both upstream and downstream of the repression sites. While expression or promoter bias appears to be common among eukaryotes, particularly higher order eukaryotes, Byrd was the first to demonstrate that this expression bias existed in *E. coli*, within its *lsr* operon. He demonstrated that the *lsr* operon is biased towards expressing genes on the *lsrACDB* flank of the operon—through both ChIP-chip microassays and through beta galactosidase activity assays[59]. Based on this data, we know that $B > 1$. Later in this study, we will use his beta galactosidase activity data [59] to fit our transcription rate constants and determine the exact value of this bias. This bias, integrated into 22, along with the definition of k_{tcA} in (23), allows us to complete our ODE for transcription (XII and XIV, for reporter mRNA).

$$k_{tcA} = Bk_{tcR} \quad (23)$$

For now, however, we must continue our discussion *lsr* operon expression with a discussion of protein production and how we will measure our outputs. Because the bias of the *lsrR* system is in the direction of *lsrACDB*, we automatically set B , for the case of *lsrR*, to 1. Therefore, in the case of *lsrR* (variables mRNA|*lsrR* and mRNA|X) become equations XI and XIII, respectively.

Ultimately, the product of the de-repression of the *lsrR* operon is the production of proteins on either side of the intergenic region of the *lsr* operon. Like transcription, the level of detail to which we will model translation (and the output of such) will depend on how much detail we actually need. Since we are not concerned with the overall mechanisms of translation, we make two assumptions. First,

translation simply happens—and that outside of the mutations that we have made in *lsrACDB* and knockouts of *lsrK*, all proteins (or monomers) are produced normally. (Had we not knocked down both genes, we would observe an increase in AI-2 phosphorylation due to the additional synthesis of *lsrK* shown in Figure 4.) Second, we assume that when *lsrA*, *lsrC*, *lsrD*, and *lsrB*—the component proteins of the AI-2 transporter, *Lsr*, rapidly polymerize into their final form and are translocated to the plasma membrane as such. We take this as an assumption since no evidence has been developed, nor mechanism has been proposed for the translocation of *Lsr* from the bacterial cytoplasm to the plasma membranes, cell walls, or capsules. Therefore, we can assume that translation of the transporter, *lsrACDB*, can be governed by a single translation rate constant, k_{tA} , and set Equation XVII to reflect our assumptions (assuming some degradation of the transporter).

In addition to translation of *LsrACDB*, we must also consider the translation of *lsrR*, which is not as straightforward as that of the transporter because *LsrR* exists in active form as either a dimer or a tetramer, as shown by Byrd and Xiu. *LsrR* is most active in its repressor role as a tetramer. Because *LsrR* is polymeric (and a homo-polymer), further steps must be taken in order to form the fully active protein. These steps will be discussed in detail in Section B.3.3.

Regardless of the functionality of our system, if we want to make our model reflect experimental reality, we must provide some output of the model that is readily understandable by experimentalists. Most microbiological experiments dealing with quorum sensing use some quantification of a change in intensity of a visual signal, whether it is the BB170 AI-2 assay, or the beta-galactosidase activity assay more

commonly used to measure bacterial gene expression. So, if the output of protein expression can be tied to a change in the output of one of those assays, further experimentation can be used to help refine the model to meet the needs of experimental research. Because the beta-galactosidase activity assay is utilized more widely, we tailor our output to that. Details of this process are discussed in the Supplementary Text (Section S2). Equations XIII and XIV, as previously discussed, describe the transcription of the reporter mRNA for either flank. Equations XV and XVI, which describe the beta-galactosidase activity in terms of bulk concentration rather than Miller Units, are identical to XVII and XVIII in form, with the exception that the functional unit, as converted in Supplemental Text S2, is converted to Miller Units (the standard activity unit in the beta-galactosidase activity assay), and that beta-galactosidase is assumed to degrade at a different rate than will either the *lsrR* monomer or the transporter.

Subsection 3.3: *lsr* Operon Repression

In order for the system to return to the original, state, the tetramer must be reformed. Here, we predict several steps based on homology to UlaR [59,77], and assumptions from previous models. First, LsrR monomer dimerizes to form the LsrR dimer (completing equation XVIII), and confirmed experimentally by Byrd and Lu, [59,77]. Free dimers then bind to the DNA at sites O1 and O2, or O3 and O4, effectively removing the *lsrRK* or *lsrACDB* available for transcription. In this model, we assume this DNA binding event occurs cooperatively with respect to our dimer. This assumption holds for any interaction between DNA and DNA-binding proteins, but we elect to only model the dimer binding step as such because cAMP-CRP binding only functions in a regulatory role. Derivations of the cooperative binding terms in equations XIX-XXI are discussed in Supplemental Text S1.

Once both dimers have bound to the *lsr* operon, we will assume at this point that there is a process, either through undiscovered assistive regulatory processes, or spontaneously, that the *lsr* operon closes back up and reforms the tetramer. This process is not cooperative, and is governed by the rate constant k_{tet} . Once the tetramer reforms, our system returns to the original state. Since we track varying bound states of the dimer, and of the availability of free *lsr* operon, we are able to monitor the overall state of our system, and the relative activity of our quorum sensing system.

Subsection 4: cAMP-CRP Module

Cyclic AMP (cAMP), a regulator which highly influences the synthesis of the *lac* operon, is an important secondary regulator within the AI-2 quorum sensing process. Several studies have suggested that knocking out the gene producing cAMP producing protein, glycerol-3-phosphate (G3P) dehydrogenase [59,78], prevents the expression of genes on either side of the *lsr* operon. Further studies suggested that cAMP caused these effects through interactions between its receptor protein, which we will call cAMP receptor protein (CRP), and genomic binding sites near the promoter sequences on either flank of the *lsr* operon, which we will call C1 and C2 (see Figure 5 for location). It has also been demonstrated, through knocking out either CRP-binding site, that the production of *lsrRK* gene products requires the binding of the cAMP-CRP complex to C1, and the production of *lsrACDBFG* similarly requires the binding of cAMP-CRP to C2[59]. In our model, we assume these binding events occur independently of the AI-2-dependent events. These binding events are shown in the diagram in Figure 7, and the equations governing these events are described by equations XXII-XXVIII in Supplementary Figure 1, which are derived based on the rate constant definitions in Table 2 as well as the events in Figure 6.

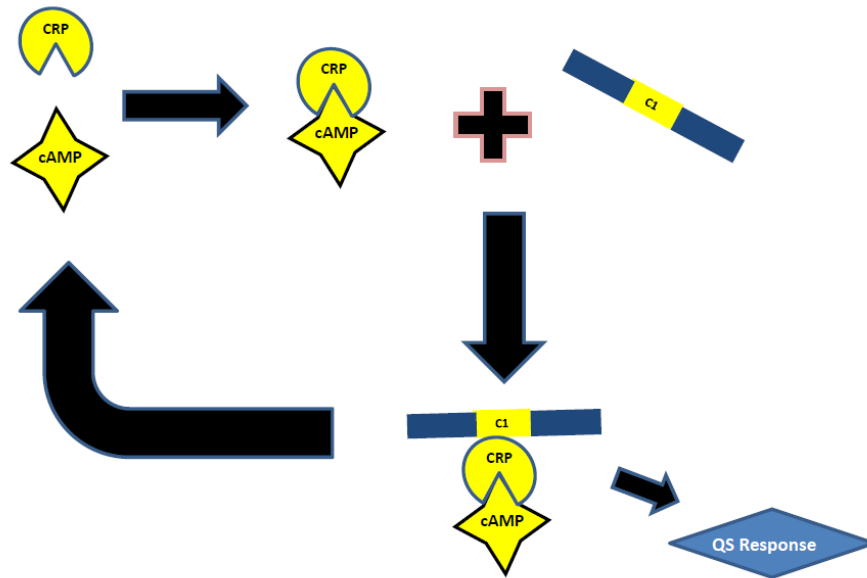


Figure 7: The cAMP-CRP module. Cyclic AMP, assumed to already be present in the bacterial cell, binds with the cAMP-receptor protein (CRP) in the cytosol. The cAMP-CRP complexes then bind the *lsr* operon at site C1 (or C2). This binding event triggers transcription of genes bidirectionally on the *lsr* operon. cAMP-CRP is then cleaved off to reform the constituent cAMP and CRP molecules.

In the case of this model, we assume a mechanism that involves cAMP-CRP binding together in the cytosol before binding to the CRP binding site shown above. However, CRP bound to C1 without cAMP bound to CRP's ligand-binding domain (LBD) can still bind to site C1. In this case, bound CRP is thought to help with the folding of the *lsr* operon and help re-form the LsrR tetramer, but further studies (yet to be published) suggest that there may be more interactions involved than previously identified. And so, we leave studying the effects of mutations of CRP sites to our future work. And for this study, we simply assume the mechanism above for the purposes of incorporating cAMP regulation into our model.

Subsection 5: Synthesis Module

In order for AI-2 to exist in real cell media, it must be synthesized somewhere. The pathway for AI-2 synthesis has been well-established in *E. coli* and appears to be conserved among many bacterial species. We discuss the pathway here, but we do not incorporate AI-2 synthesis into our model as a part of this work. Rather we will incorporate the AI-2 synthetic pathway in a future extension of our model. The main pathway is relatively simple. Methionines are converted to S-adenosylmethionine (SAM) by the enzyme MetK. This is followed by the demethylation of SAM by the enzyme CheR (in the presence of a methyl acceptor) to form S-adenylhomocysteine (SAH). SAH is then hydrolyzed by the enzyme Pfs to form S-ribohomocysteine (SRH). The enzyme LuxS, knocked out in our study, then converts SRH to an AI-2 precursor known as 4,5-dihydroxy-2,3-pentanedione (DPD), which is unstable and immediately converted into one of several more stable isomers which are known as AI-2.

Each step in this process is regulated by a number of means. At the SAM to SAH step, the enzyme SpeD can compete with CheR (or a similar SAM-demethyltransferase) for SAM. Instead of SAM being converted to SAH, SAM could be decarboxylated and converted to the alternative product MTR, as well as spermidine and adenine[79]. At the SAH to SRH step, cAMP can upregulate this step by increasing the synthesis (and thus availability) of Pfs[63,79,80]. Conversely, because cAMP is often synthesized as a signaling molecule in *E. coli* in low-glucose conditions, this conversion of SAH to SRH is downregulated in the presence of high intracellular glucose concentrations. At the SRH to DPD level, cAMP and glucose

carry out opposite effects based on increasing or decreasing the expression (and production) of LuxS—except in that LuxS expression is positively correlated to glucose concentration (rather than to cAMP, as with Pfs expression).

Even in conditions that are supposed to mean high optimal AI-2 synthesis inside the cell, depleting the cells of iron(III) ions (or LuxS in cell-free media of iron(III) ions), depletes the concentrations of AI-2 that are synthesized. [81]

Therefore, it is implied that iron(III) ions activate LuxS by binding to some regulatory site on LuxS.

Section 3: Model Implementation and Calibration

Subsection 1: Calibration of Transcription Constants k_{tcR} and B

One of the main goals of the model we are developing is to explain and simulate experimental data. And in order for our model to be supported by experimental data, we must be able to fit our parameters to some sort of real data. In the absence of methods to test a lot of our kinetic parameters, we utilize output features from previously published data (Byrd, 2011). Since the only temporal domain data we find refers to the expression of *lsrRK* and *lsrACDB* in Miller Units, we must calibrate our model accordingly. For all intensive purposes, we assume that translation is governed by the rate constants k_{tl} and k_{tlA} , which are each set to 1 min^{-1} . So, we utilize the output data to determine our transcription rate constants k_{tcR} and B .

To determine k_{tcR} , we first assigned a starting value of $k_{tcR} = 0.1 \text{ min}^{-1}$ and $B = 1$ (assuming zero transcriptional bias in our system). We then implemented our ODE system with k_{tcR} varying from our preliminary value of 0.1 min^{-1} to 1 min^{-1} . Then, we extracted our data points that matched the time points from Byrd's activity unit data. Due to the adaptive step-size utilized by MATLAB in order to compute the numeric integral, an exact match between the time point in Byrd's work [59] (approximated and reproduced in Figure 8) and that in the data point may not be found. So to compensate, we find the time point in our model simulation that is closest to the particular time points in the data (with the least amount of error). We then find our beta-galactosidase activity at those time points based on the system we have just

integrated (See Section B.6.2. for how it was implemented), and compile them into a row vector the same length as our experimental time vector.

Once we have these data points, we selected our k_{tcR} by calculating R^2 values between the model with the k_{tcR} in question. R^2 is a statistical measurement which determines how well data fits to a particular model, or how well a particular model fits to a known set of data. We define R^2 as a metric to test the latter, and we calculate it via the calculations in (24) through (26).

We start our calculation by defining our vector of β -galactosidase activity data (without considering which flank we are considering right now) $\bar{\mathbf{Y}}$, and the predicted β -Galactosidase activity data from our model at a particular k_{tcR} , \mathbf{Y} . We can now define our error vector, $\boldsymbol{\varepsilon}$ with a length L (also equal to the length of the time vector from the Byrd data), by vector equation in 24. (These errors can also be called residuals.)

$$\boldsymbol{\varepsilon} = \mathbf{Y} - \bar{\mathbf{Y}} \quad (24)$$

In the first step to normalizing the error, we find the sum of the square of the error, SSE, as shown in (25), for our error vector $\boldsymbol{\varepsilon}$ by squaring each element (ε_i) and adding the elements together.

$$SSE = \sum_{i=1}^L \varepsilon_i^2 \quad (25)$$

In order to compare this error with the variance within our data, we now compute the total sum of squares of our data in $\bar{\mathbf{Y}}$, SS_{total} as shown in (26), where $Var(\bar{\mathbf{Y}})$ is the variance of $\bar{\mathbf{Y}}$

$$SS_{total} = (L - 1)Var(\bar{\mathbf{Y}}) \quad (26)$$

We now can compute R^2 as shown in (27).

$$R^2 = 1 - \frac{SSE}{SS_{total}} \quad (27)$$

We note a few key observations. If $SSE > SS_{total}$, we observe that our R^2 value will be negative, meaning that we cannot use our model to predict our data. Thus, we reject k_{tcR} values that produce an $R^2 < 0$. Likewise, if $SSE = SS_{total}$, we will have an $R^2 = 0$, which represents random correlation. Because of this, we also reject any k_{tcR} which results in $R^2 = 0$. Therefore, the first class of k_{tcR} values we accept are those with $R^2 > 0$. Because of our definition of R^2 (and that SSE and SS_{total} cannot be negative), the maximum R^2 we obtain would be $R^2 = 1$, which defines a perfect fit to our data. Because of this, we select our k_{tcR} based on which k_{tcR} produces the highest R^2 value, when compared to our data.

After the initial round of implementing this algorithm and rejecting the negative R^2 values, we identify the k_{tcR} values such that R^2 went from increasing to decreasing, and used those k_{tcR} values to refine our estimate for k_{tcR} . When we could not improve our R^2 value any further, we selected the k_{tcR} that produced the highest R^2 value.

After selecting a k_{tcR} value, we hold k_{tcR} and vary our transcriptional bias B over a pre-defined range, and select our B using a similar protocol to the one we just described for selecting k_{tcR} , except utilizing the k_{tcR} we had previously estimated.

As we will demonstrate in Section 3.2.2 (Chapter 3, Section 2, Subsection 2), this approach will form the basis of how we might utilize our model to demonstrate the effects of specific mutations.

Subsection 2: General Model Implementation

In order to solve our model, we needed to select a program that could integrate our model in an accurate, yet computationally efficient manner. To do this, the models were implemented using the constants in Table 1, the initial values in Table 2, and in MATLAB (Mathworks, Inc.) and integrated using MATLAB's ODE23s algorithm. (ODE23s is one of many ODE numerical integration algorithms that comes prepackaged within the MATLAB software package, which uses a low-order ($n=1$) Runge-Kutta method which is capable of handling stiff systems. Higher-order non-stiff algorithms may have provided a higher-accuracy solution by running a higher-order Runge-Kutta integration step, we found that these higher-order nonstiff methods, with regards to integrating our 28-equation ODE system, too computationally expensive to be integrated on a standard 64-bit personal computer.)

Subsection 3: Implementation of Sensitivity Analysis

Sensitivity analyses are useful tools to understand how a system would change in response to the changing biological conditions of a system, or what would happen to our system under differing conditions for rate constants. For linear systems, this process is relatively simple. We would first find all our equilibrium points (solving our mass matrix $dYdt = 0$, where Y represents then entirety of our ODE system as shown in Figure A). Then, we would find the Jacobian of that matrix and find the eigenvalues and/or eigenvectors of the resulting matrix. We could then plug in our equilibrium points to determine the stability of our system at those points. If the real parts of eigenvalues are all negative, the equilibrium (or steady-state) points are all

stable at those conditions. If any eigenvalue is zero then we cannot determine the stability of the system at that point. If any eigenvalue has a positive real component, the system would be marginally stable at best (if every other eigenvalue is negative), and likely to be unstable. Discriminant analysis can be used to determine the ranges of each rate constant that could predict the behavior of the system. However, in large systems, discriminant analysis becomes complicated and computationally expensive.

And for large nonlinear systems, no standard algorithm for determining stability points exists. Even if one existed, completing one for a 28-D system may be more computationally expensive than simply evaluating the ODE system over a period of time, simply changing one particular constant. And so, we perform our sensitivity analyses by varying our rate constants within a range that we predefine. For our system, this may represent a certain fold increase or decrease in transcription rate of our gene, in dimerization rate of a protein, or affinity of a protein for DNA (in the form of dissociation constants). How this increase or decrease in each rate constant depends on how we define them to begin with. As we show in sections C.3. and C.4, modifying the value of a constant or form of transcription influence the behavior of our system, not just with the immediate effects, but with state variables that are further downstream.

As to some applications of our sensitivity analysis, we might want to know what happens with expression of *lsr* if we reduced or amplified the affinity of the LsrR binding sites for LsrR, citing situations in which we might make a point mutation experimentally to demonstrate the effects of such. Or, we might want to

track primary and secondary effects of changing the rate at which a regulatory or primary reaction process might happen.

Chapter 3: Results

Section 1: Fitting the Basic Model Shows a Dynamic Response to the External AI-2

System

Using the equations in Figure A and the constants in Tables 0 and 1, we created a base case for the model to determine how our control would respond over time.

Figure 8 shows the general response curve of the AI-2 phosphorylation-dependent equations as a response to our AI-2 and ATP input (a). As the intracellular (and extracellular) AI-2 concentration in our system increases, we see an increase in the production of both products including AI-2-P (shown in (c)), and ADP (shown in (b)). As AI-2 concentrations fall off, AI-2-P and ADP production stop and the concentration-dependent degradation of ADP and AI-2-P start to dominate. The peak in AI-2-P concentration occurs at $t=400$ minutes and has a full width half maximum (FWHM) of ~ 240 min, roughly the same time at which our fitted AI-2 concentration curve peaks but a larger FWHM. The FWHM of AI-2-P curve, is smaller than that for ADP (FWHM = 350 min) because AI-2-P, as has been well established, drives the cleavage of the lsrR tetramer.

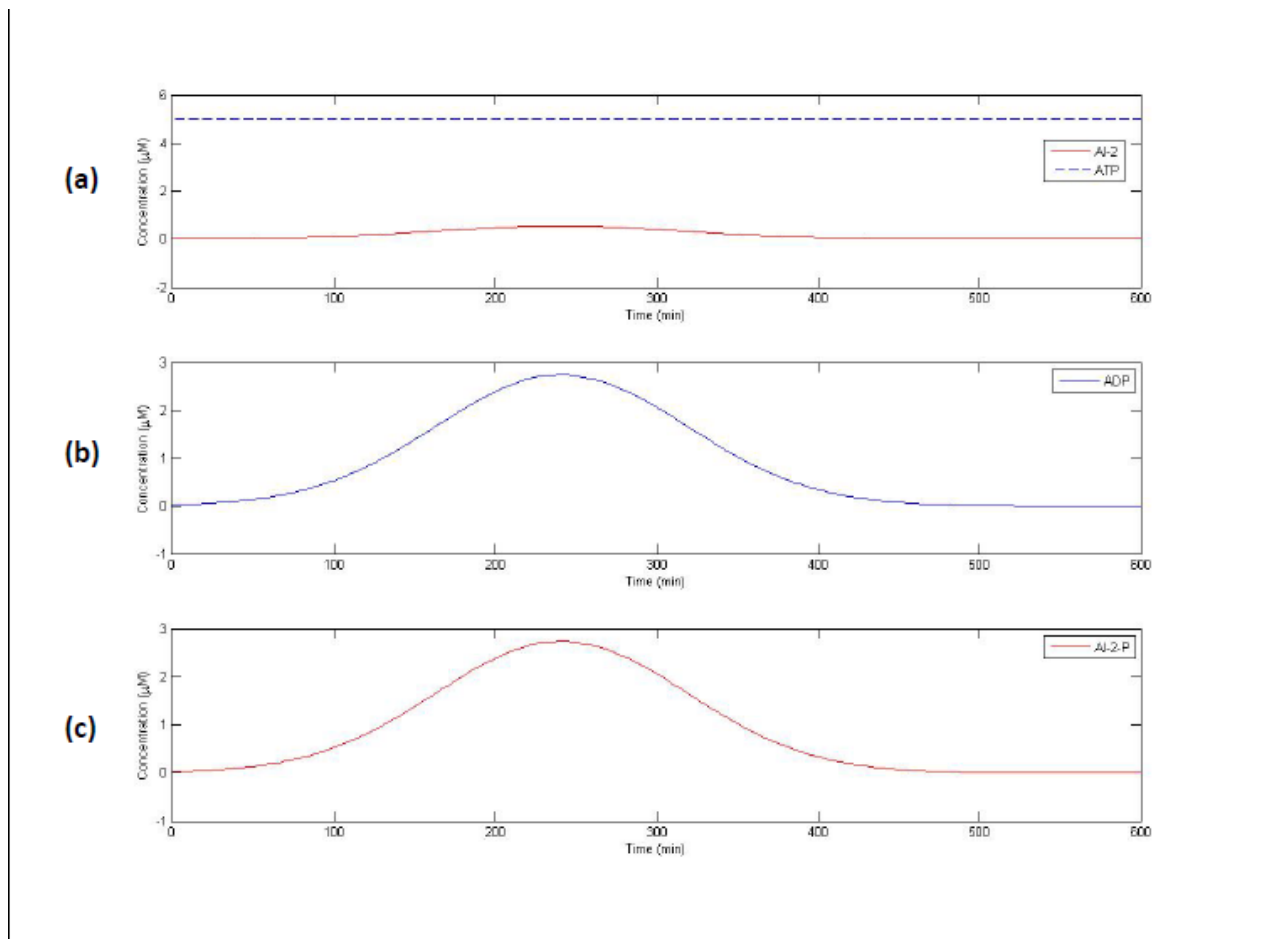


Figure 8: Dynamics of *lsrK*-dependent phosphorylation reactions. The dynamics for the *lsrK*-dependent phosphorylation of AI-2 is shown over a simulation period of 1000 minutes. Our input ATP and AI-2 concentration profiles are shown in (a). The *lsrK*-catalyzed reaction between ATP and AI-2 produce the ADP (b) and AI-2-P (c) in the manner shown.

Fittingly, as the plots in figures 9a-d suggest, the resulting AI-2-P dephosphorylation can be tied to decreases in tetramer concentration. When we examine tetramer concentration in the presence of AI-2, we observe that as AI-2 increases, our tetramer concentration decreases from our initial value of 20 molecules/cell (20 copies of the *lsr* intergenic region (as well as *lsrR* and *lsrACDB*)) to almost zero when AI-2 concentration hits its peak, and rises again back towards the original state as AI-2 (and AI-2-P) is depleted. The plots in figure 9c and d, highlight that the bound

phosphorylated lsrR dimer and free phosphorylated dimer concentration profiles follow the patterns we see for our AI-2-P and tetramer curves. When the free AI-2-P-dimer complex appears, we also see a similar appearance in the free (de-repressed) *lsrRK* gene or free (de-repressed) *lsrACDB* gene in equal magnitude, as shown in Figure 10. The concentrations of those free genes increases with increasing AI-2 at roughly the same time point, and then decreases as AI-2 (and AI-2-P) become less available, and as synthesized dimer binds to the free genes.

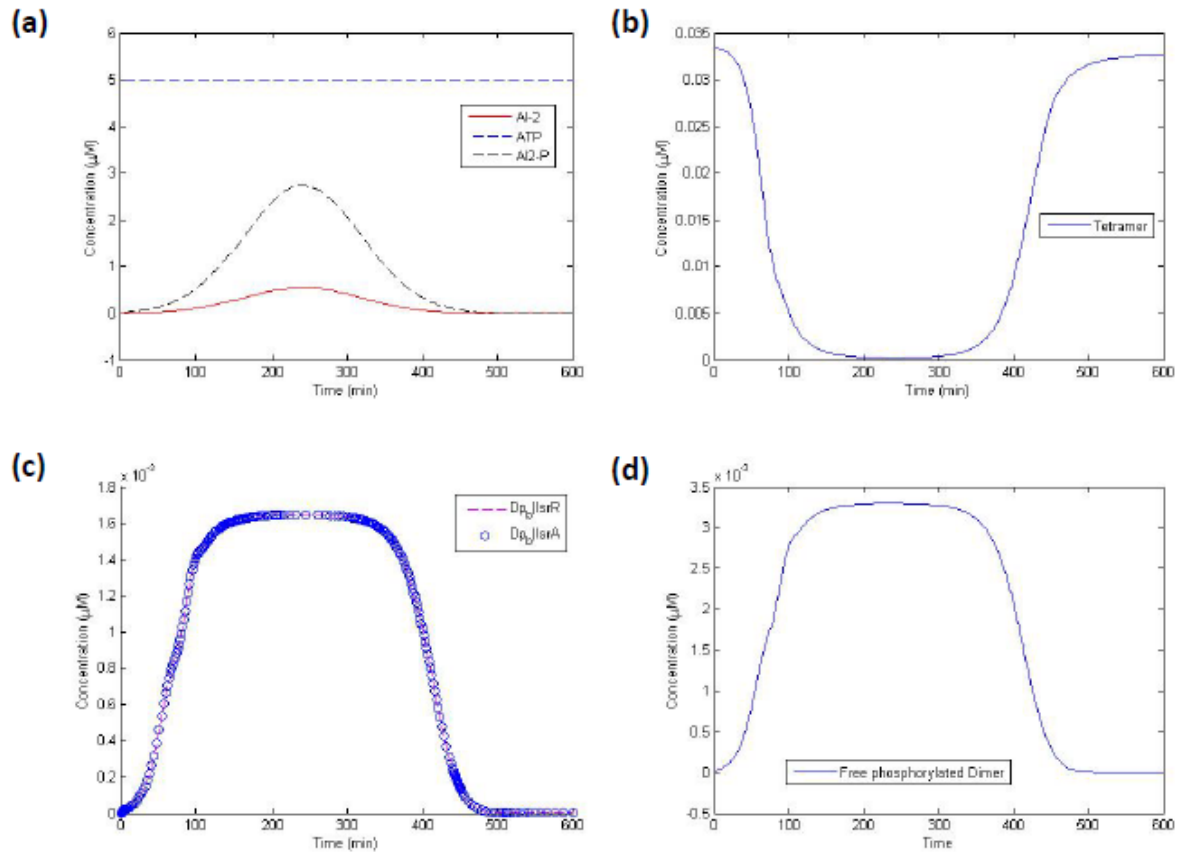


Figure 9: Tetramer cleavage reactions. The lsrR tetramer (b, in blue) is dephosphorylated in response to the input AI-2 and ATP, and subsequently AI-2-P concentrations in (a). When AI-2-P binds to the lsrR tetramer, it initially forms an immediate AI-2-P/lsrR dimer complex that is bound to binding sites O1 and O2 ($Dp_b|lsrR$), and O3 and O4 ($Dp_b|lsrA$) in the *lsr* regulon as shown in (c) (scale: 1×10^{-6} μM). Since these complexes may not be stable when attached the lsrR binding sites,

AI-2-P/LsrR dimer complexes (phosphorylated dimers) (d) break away from the aforementioned binding sites.

When the *lsrRK* and *lsrACDB* genes are transcribed (as well as the mRNA genes) they follow a similar profile to everything else. They increase to peaks at around $t = 240$ minutes and decrease back down to a steady state close to zero for the rest of the simulation (though the decrease does not really happen until after $t=360$ minutes). The general profile of mRNA synthesis also translates to the production of Lsr, and the monomer form of LsrR, as expected. However, the relative profiles of beta galactosidase (check for beta galactosidase everywhere in the thesis to make sure it's the same everywhere – hyphen no hyphen etc... activity in both *lsrR* and *lsrA* directions, as shown in Figure 12, follows more of a sigmoidal profile, reaching an equilibrium state when AI-2 is depleted, since we do not include a degradation term for beta galactosidase. Some modifications to the mRNA transcription terms are discussed in the sensitivity analysis in section C.3. We also consider the allosteric regulator cyclic AMP (cAMP) and its influence on expression of *lsrR* and *lsrACDB*. Furthermore, these similar observations extend to the synthesis of AI-2 transporter (Lsr), shown in Figure 11 and reflected in the beta-galactosidase activity data in Figure 12, since the transcription and translation of *lacZ* attached to either *lsrR* or *lsrA* is controlled by the same promoters controlling transcription and translation of LsrR and LsrACDB (Lsr).

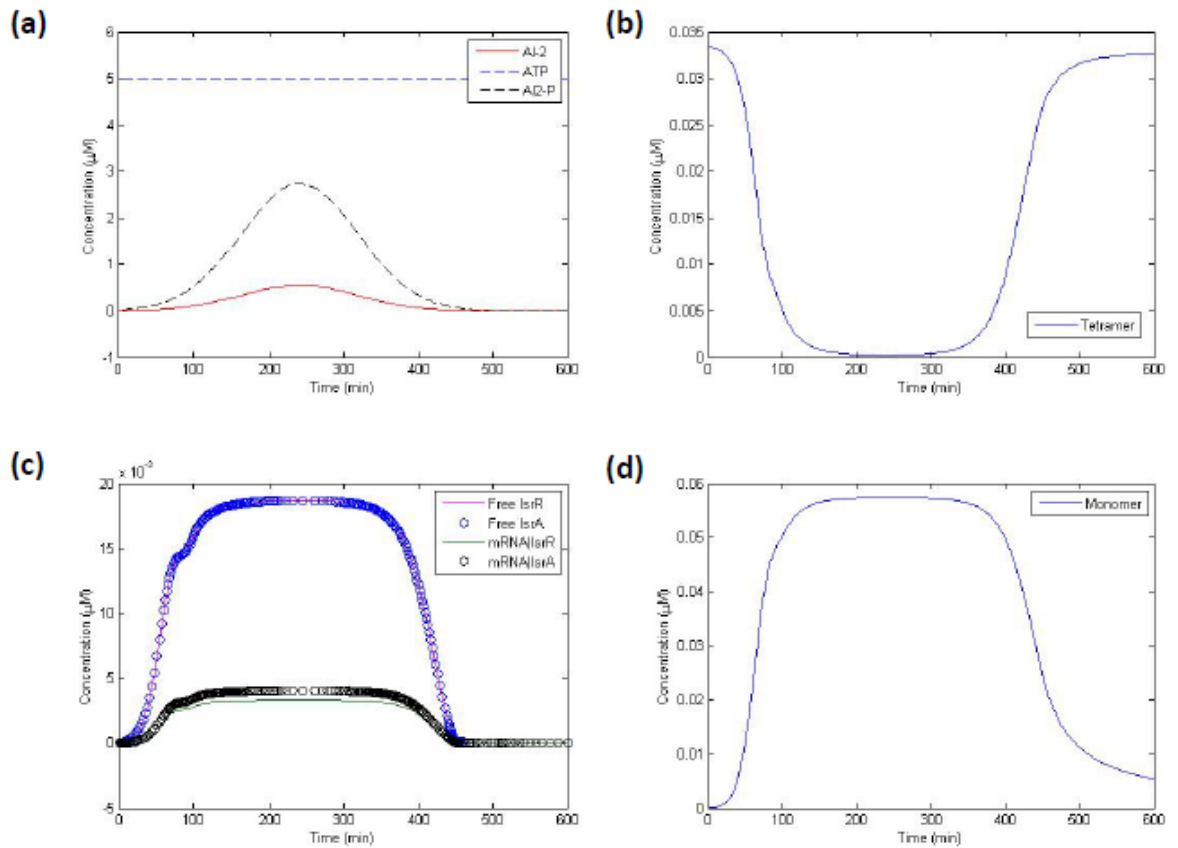


Figure 10: *lsr* operon de-repression and LsrR monomer synthesis. The de-repression of *lsrR* and *lsrA* to free states (c) and the transcription (c) and translation of the *lsrR* mRNA to *lsrR* monomer (d) in response to AI-2-P input (a). Figure (b) shows the concentration of *lsrR* tetramer in our system, that its derepression by the binding of AI-2-P is tied to the increase in the rate of de-repression of *lsrR* and *lsrA* and the production of *lsrR* monomer. Scale for mRNA concentration in (c) is $10^{-3} \mu\text{M}$.

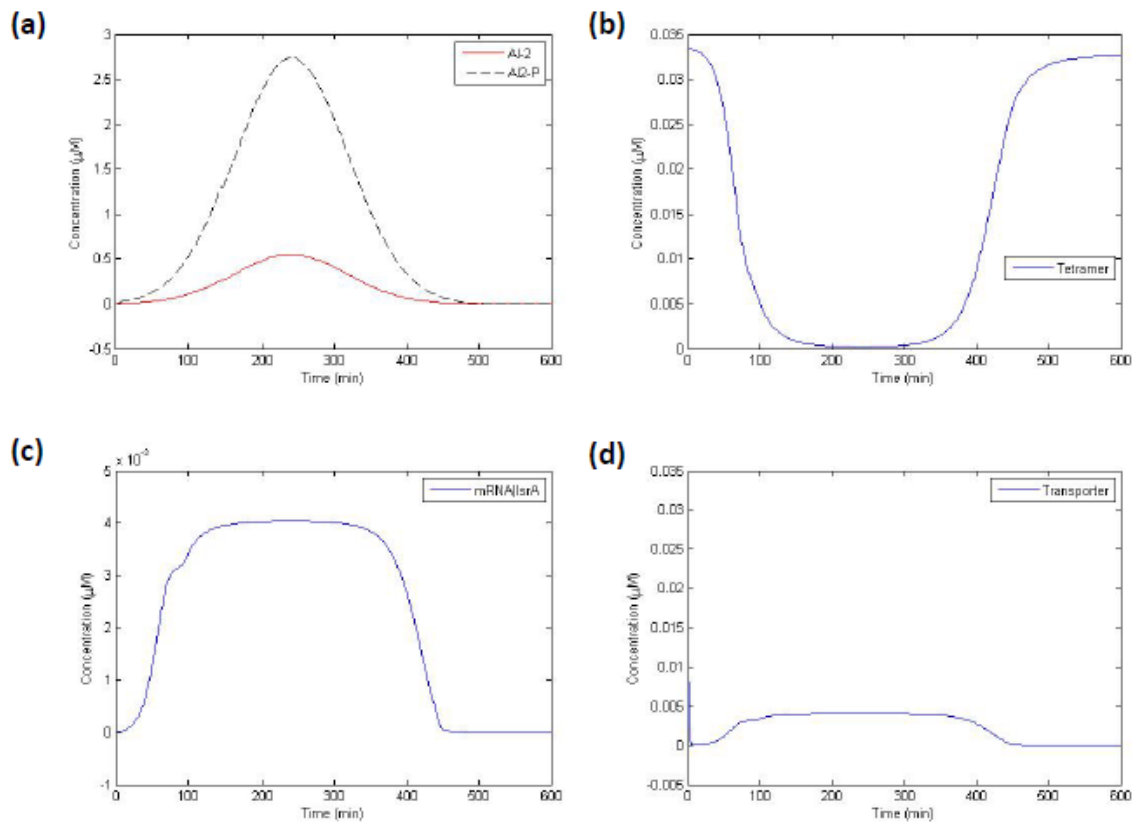


Figure 11: Production of *lsrR* transporter in the model. Production of the lux-S regulated transporter Lsr from *lsrACDB*. AI-2 phosphorylation (a), besides activating the transcription and translation of *lsrR* monomer, also induces the production of mRNA transcripts of *lsrACDB* (c) which produces Lsr (d). Scale for mRNA concentration in (c) is 10^{-3} μM .

This base model was fitted to Byrd’s transcription data up to $t=10$ hours (and ignoring the overnight culture) using an R^2 -based algorithm previously described in Section B.6.1. The fit values for this “base case” are shown in Figure 13. These points, along with the transcription of the associated mRNA of the beta galactosidase genes associated with *lsrR* and *lsrA*, are shown in figure 12 (c) and (d), in correspondence to the variable AI-2 and AI-2-P input (a) and LsrR tetramer that represses our system. The beta galactosidase activities, unlike LsrR monomer and transporter synthesis, flat-lines when AI-2 is depleted (rather than decreasing to zero

concentration). But, like in the monomer and transporter concentrations, they appear to start to reach an equilibrium level in the absence of AI-2 at $t > 240$ minutes. And so, in the base case, the fit to Byrd's dynamic data with a wild type insert of *plsR14* and *plsR26* (plasmids containing the wild type intergenic regions with *lacZ* reporters expressed in either the *lsrA* direction or the *lsrR* direction)..

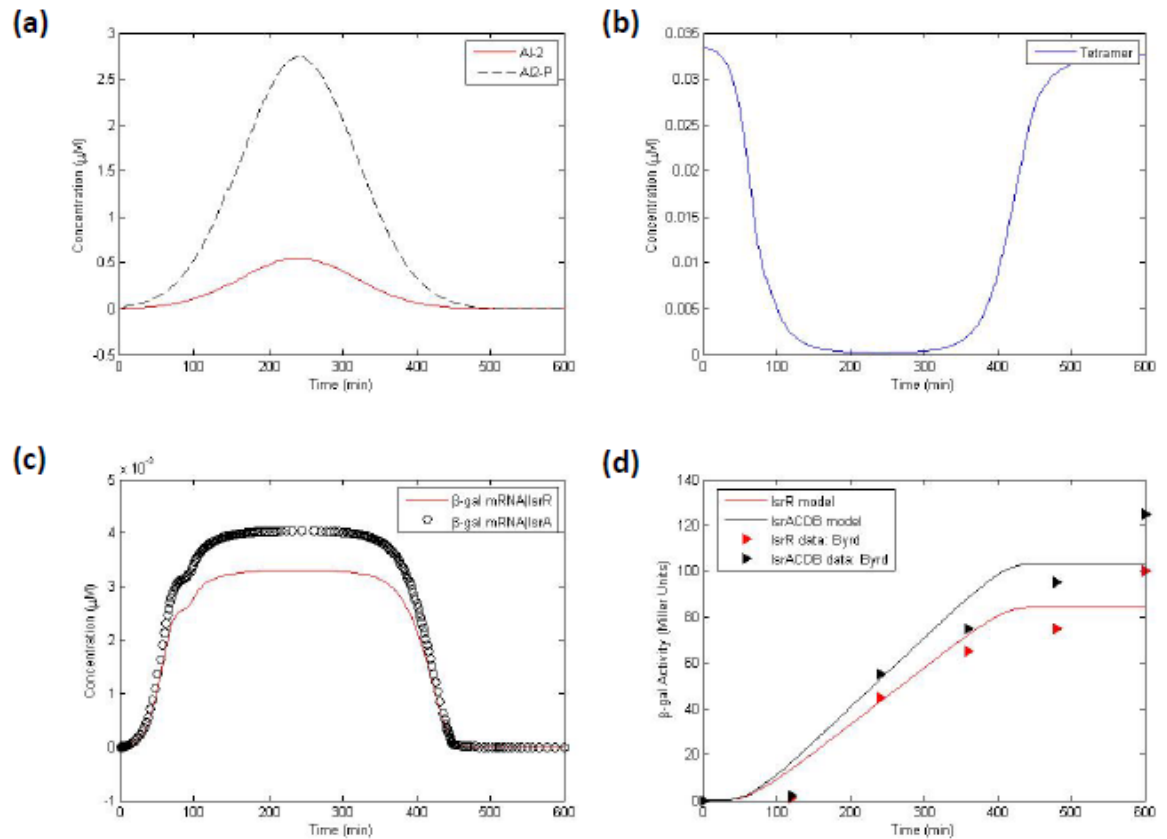


Figure 12: Beta-galactosidase activity associated with de-repression of the *lsr* operon. (a) shows the input AI-2 and resulting AI-2-P concentration profiles we fitted before. (b) shows the dynamic response of the *lsrR* tetramer concentration. (c) shows transcription of *lacZ* reporter genes attached upstream of either *lsrR* and *lsrACDB* (scale is 10^{-3} μM mRNA), and (d) shows the beta galactosidase activity that results from AI-2 activation in Miller Units. The points from Byrd (filled-in triangles) are shown to represent the fit that was utilized for our transcription constants.

FITTED PARAMETER	VALUE	R ²
k_{tcR}	2.1 min ⁻¹	0.9321
B	1.225	0.9250

Figure 13: Estimated values of k_{tcR} and B

To close the loop on our system, the *lsrR* monomers dimerize to form free *lsrR* homodimers. The dynamics of this part of the loop are shown in Figure 14. *LsrR* monomer concentration follows a profile similar to that of the mRNA concentration profile for *lsrR*, in that it increases to a peak value, stays close to that peak value until AI-2 is partially depleted, and then decreases back to zero rapidly as AI-2 is further depleted. The free *LsrR* dimer concentration, on the other hand, appears to form a flat line until approximately $t = 360$ min, after which it starts increasing to an equilibrium value beyond the 10 hour simulation. This odd event is highlighted by the concentration profiles of *LsrR* dimers bound to the putative binding sites in figure 14d (which follow each other). This observation suggests that the formation of the free *LsrR* dimer could be a rapid step until the putative binding sites reach saturation. The rapid increase (and eventual equilibration of) *LsrR* tetramer concentration confirms that the AI-2 depleted system reaches equilibrium. And by the end of the simulation, most of the available bound dimers have re-formed the initial concentration *lsrR* tetramer, corresponding to a near-zero concentration of AI-2. Several studies suggested that this simple folding of the tetramer does not happen simply from *lsrR* dimers binding to both sets of putative binding sites. Rather, it is believed that CRP, when bound to C1 and C2, may assist in the folding of the *lsr* intergenic region forming the hairpin loop that may facilitate the reformation of the

lsrR tetramer. In Figure 15, we consider the cyclic AMP dynamics of our system. In our model, we assume CRP binding, or more specifically cAMP-CRP binding, to the CRP binding sites C1 and C2 in our system. All components of this system reach equilibrium with each other, suggesting that there will always be cAMP-CRP complexes that are bound to C1 or C2 (or both) at any point in the simulation. This may assist both the folding of the *lsr* intergenic region and the derepression of *lsrR* and *lsrACDB*. That is, we do not describe CRP dynamics in the current model.

The dynamics of the CRP-related module (cAMP module) are shown in Figure 15, and suggest that the binding of cAMP-CRP complexes to CRP binding sites (as shown in figures 15c-d), as well as the formation of CRP complexes (15c) appears to be AI-2 independent (shown in 15a and b), as well as independent of the breaking apart of *lsrR* tetramer. However, figure 15e) suggests that while the actions appear to be independent, only a small concentration of CRP binding sites appear to be occupied despite excess cAMP and CRP present in our simulated sample. And so, we do not know enough from this base case to necessarily confirm the regulatory role of cAMP in influencing the dynamics of *LsrR* (in its several forms).

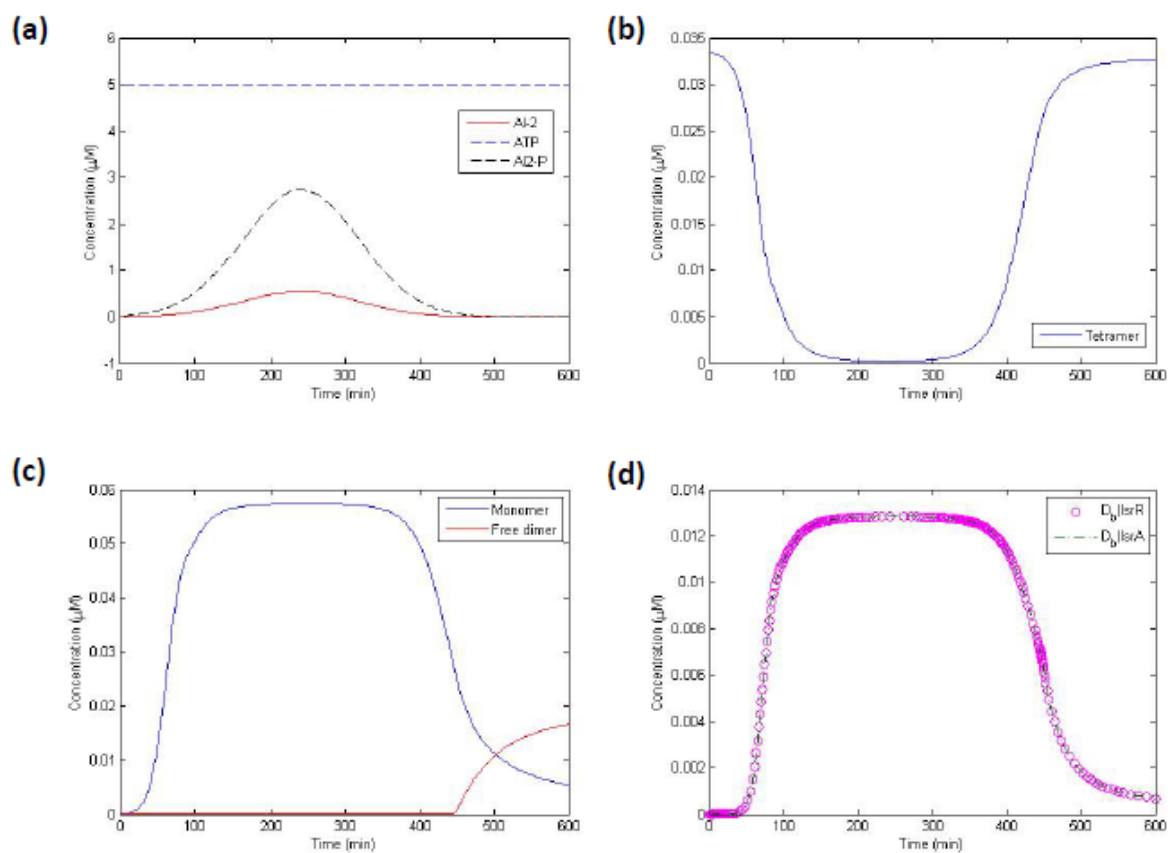


Figure 14: Re-formation of the tetramer. Dynamics of the re-formation of the LsrR tetramer (b) in response to AI-2 and ATP, and consequently AI-2-P input (a). Increases in AI-2 lead to a significant decrease in LsrR tetramer, which leads to the synthesis of LsrR monomer (c). The monomers in (c) then form a homodimer (shown in c), which then bind to the putative binding sites O1/O2 ($D_b|l\text{s}rR$) or O3/O4 ($D_b|l\text{s}rA$) (d). An increase in free LsrR dimer occurs at $t=450$ min due to the started saturation of putative binding sites.

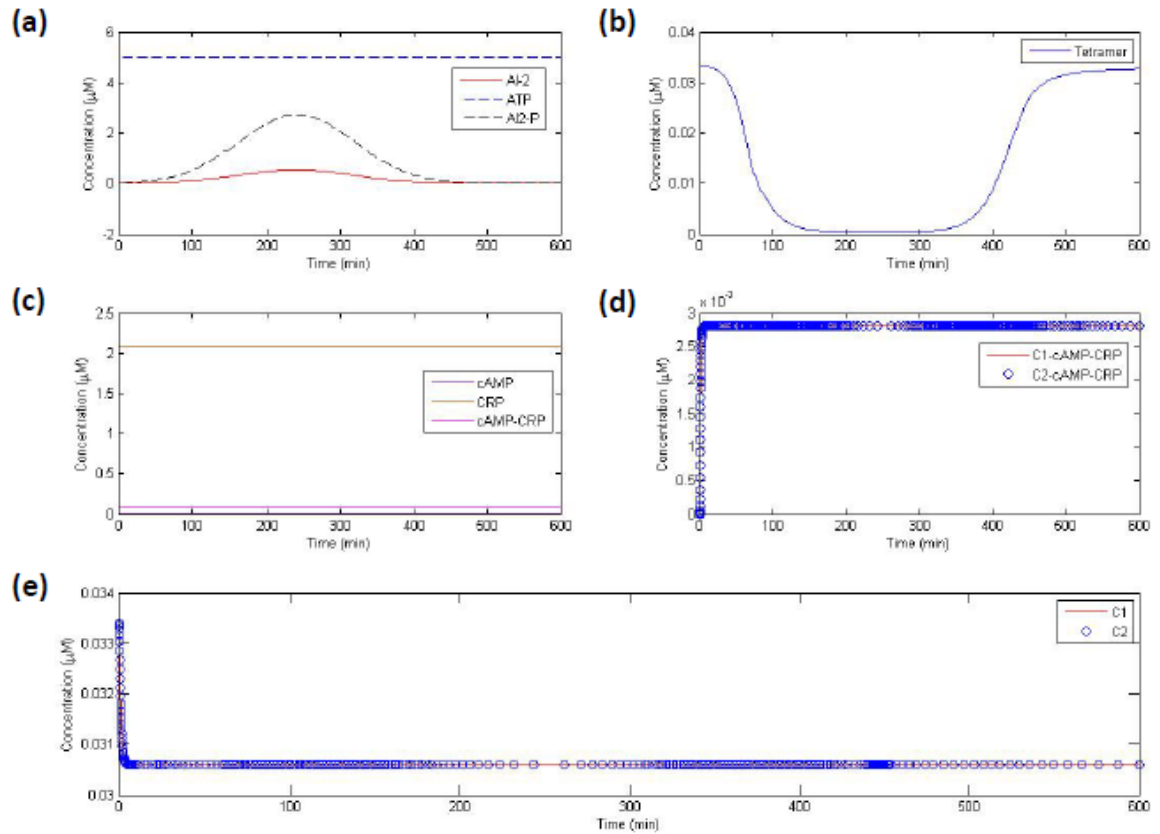


Figure 15: Cyclic AMP regulatory dynamics. Cyclic AMP (cAMP) and CRP initially form cAMP-CRP complexes (c). This reaction, not being dependent on AI-2 and ATP concentration (a) or tetramer concentration (b), moves to rapid equilibrium. (d) tracks the concentration of cAMP-CRP complexes bound to CRP binding sites C1 and C2. (e) shows the dynamics associated with the free CRP binding sites (C1 and C2). All concentrations are bulk concentrations defined in μM .

Section 2: Adjustments to the Model

The basic model may be the first model of the *lsr* operon that takes into account the molecular dynamics of LsrR and its interactions with the operon. We reveal further dynamics of the model through a generalized sensitivity analysis of two different parameters $K_{\text{bind}}|\text{lsrR}$ and $K_{\text{bind}}|\text{lsrA}$, and model specific effects of particular mutations of various binding sites through their effects on specific binding parameter. $K_{\text{bind}}|\text{lsrR}$ and $K_{\text{bind}}|\text{lsrA}$ are micro-dissociation constants that govern the binding of the LsrR dimer to either the O3/O4 half-sites ($K_{\text{bind}}|\text{lsrR}$) or O1/O2 half-sites. The *lsrR* or *lsrACDB* genes are considered repressed in one direction once the LsrR dimer binds to the set of half-sites in the direction of gene expression in which we are interested. (More on this matter will be discussed in Section 3.2.2.)

Subsection 1: Effects of Specific Mutations

Previous studies by Byrd and others suggested that specific mutations to different genes within the *lsr* operon had differing effects in affecting the bidirectional expression of the *lsr* operon. To demonstrate such effects, we examined several such mutations—the *lsrR* knockout mutation, which we identify as CB11, and various binding site mutations—the putative binding sites O1, O2, O3, and O4, whose mutations we attempt to reflect by fitting $K_{\text{bind}}|\text{lsrR}$ and $K_{\text{bind}}|\text{lsrA}$ to the WT conditions. But before we begin discussing those results, we had to define our CB11 conditions to reflect basal transcription, and then reflect those realities.

Subsection 1.1: The *lsrR* Knockout (CB11 strain)

As mentioned in the previous section, Byrd developed a strain of *E. coli* K12 that were *lsrR* knockouts. In his experimental studies, he found that expression of *lacZ* reporter genes in either direction were significantly higher than in similar wild type strains (expressing *lsrR* normally). In our simulation, we reflected the CB11 mutation by defining a new protein translation constant k_{tlM} , which in the wild type case, is equivalent to k_{tl} . In CB11, $k_{tlM} = 0$. We also set $T_b = 0$, and $lsrR = lsrA = N * 0.00167 \text{ uM}/(\text{mol}/\text{cell})$ (calculated in Supplementary Text S2), where N is our copy number.

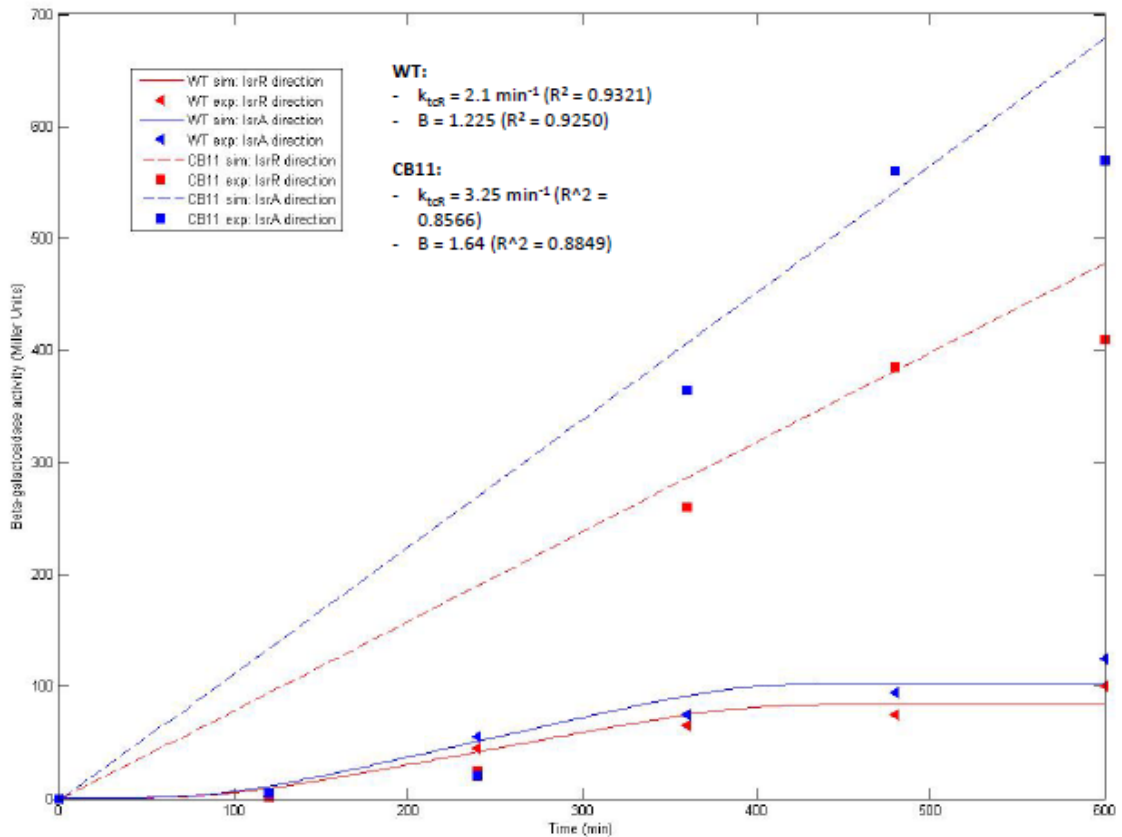


Figure 16: Wild type and *lsrR* knockout (CB11) fitted over time.

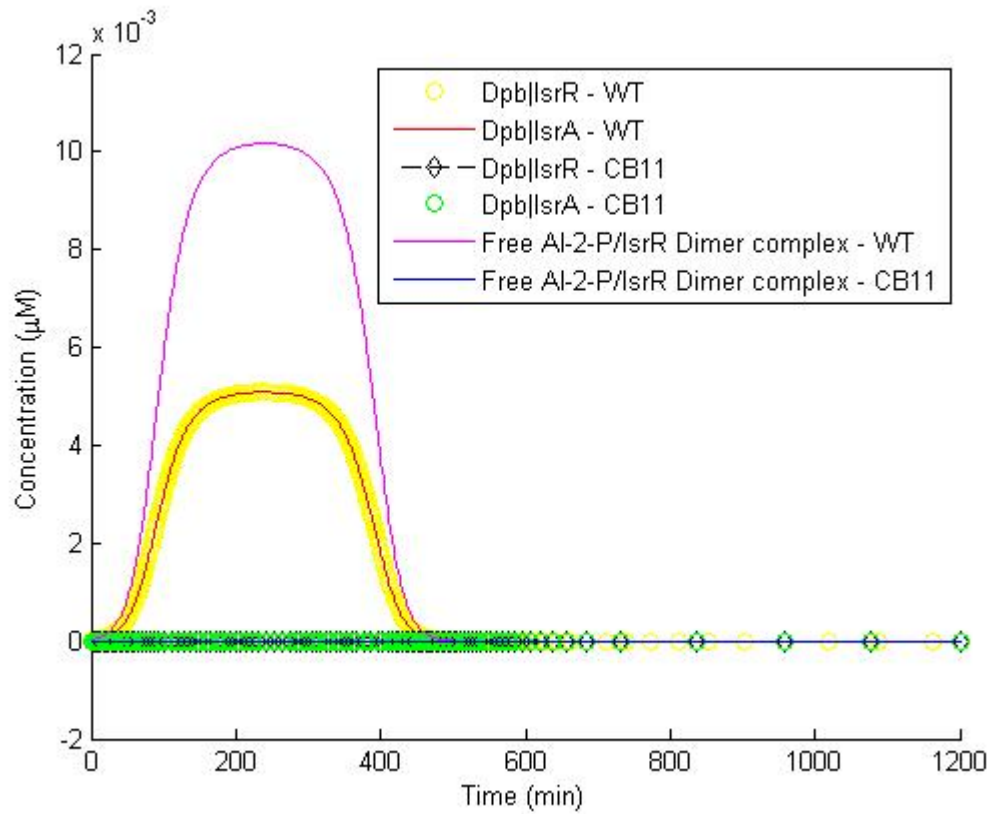


Figure 17: *Isr* operon de-repression intermediates in wild-type (WT) and *IsrR* knockout (CB11) conditions

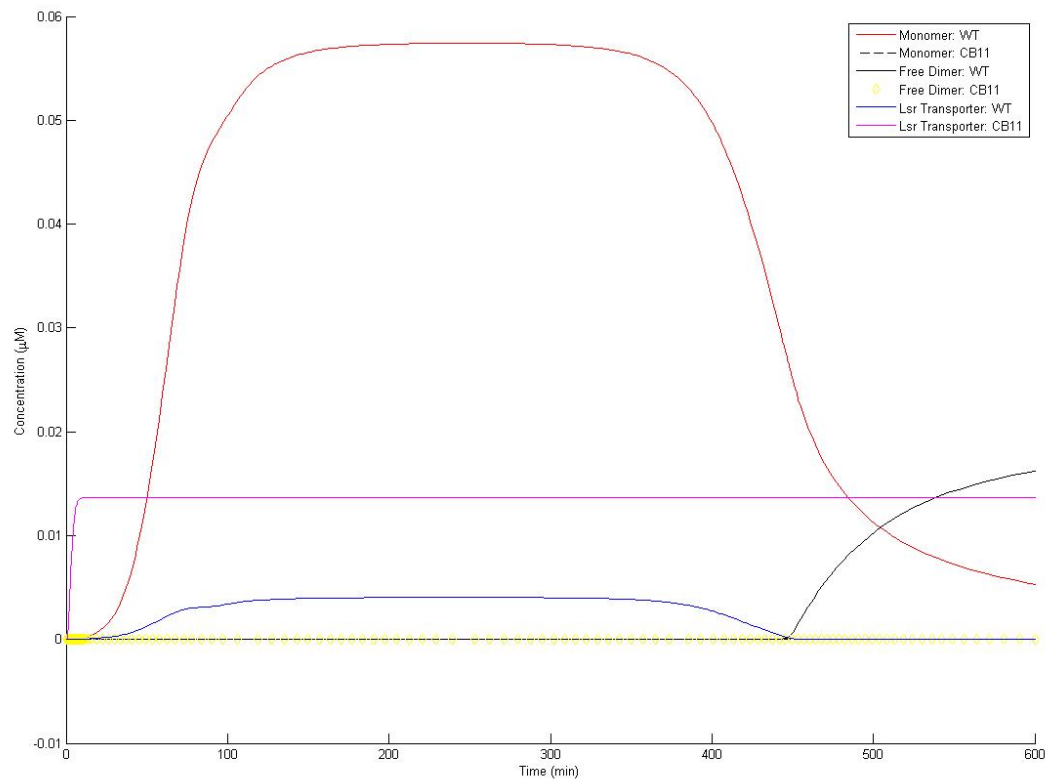


Figure 18: Wild type and *lsrR* knockout dynamics of LsrR and LsrACDB protein products.

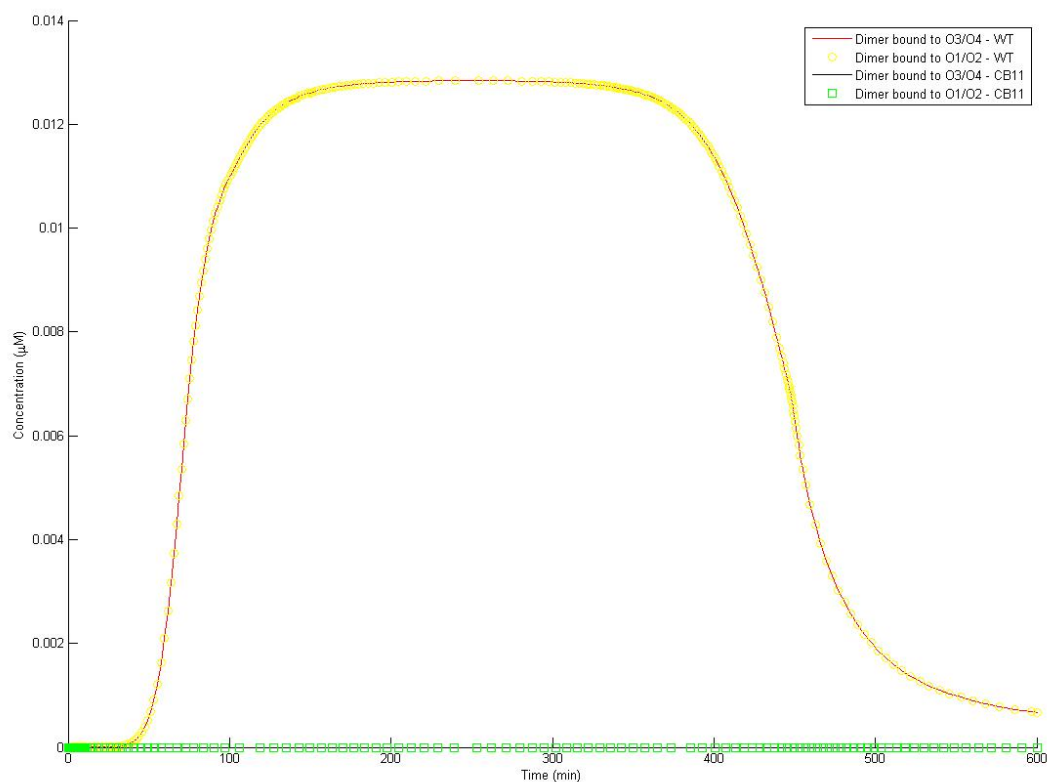


Figure 19: Bound dimer differentiation in wild type and *lsrR* knockout (CB11) conditions.

As we expected, and as shown in Figures 17 through 19, we do not see any significant concentration of LsrR products in the CB11 system. We see several features. First, mRNA concentrations in reporters and genes in both directions (including the garbage “knockout mRNA” reach a non-zero steady-state in the CB11 case, rather than return to zero as they would in the wild type. This is consistent with permanent derepression of the *lsr* operon. Second, we observe that Lsr transporter concentration reaches a non-zero equilibrium state, in absence of LsrR-dependent repression. Third, and probably most significantly, we observe that beta-galactosidase activity moves from a sigmoidal profile that reaches a steady state to a linear profile that keeps increasing. When fitted using Byrd’s temporal data using our R^2 -based

algorithm, we find that we can fit that data best with $k_{tcR} = 3.25 \text{ min}^{-1}$ ($R^2 = 0.8566$) and $B = 1.64$ ($R^2 = 0.8849$).

Subsection 1.2: Reflecting Real Mutations in the Model

One application of our model might be to examine the effects of particular mutations within the *lsr* intergenic region on the expression of our operon. As previously stated, our model is the first model to consider the molecular dynamics of the LsrR repressor, rather than simply a “quorum sensing switch” in the Lsr quorum sensing system. We previously suggested how theoretically how adjusting our micro-dissociation binding constants could affect the expression of the *lsr* operon, raising expression levels in both directions.

We test this assumption by simulating model systems in which plasmids containing mutations of different combinations of binding sites have been inserted into the genomes of *E. coli* K12 bacteria. A summary of the mutations is listed in Figure 21, and in graphic form in Figure 20.

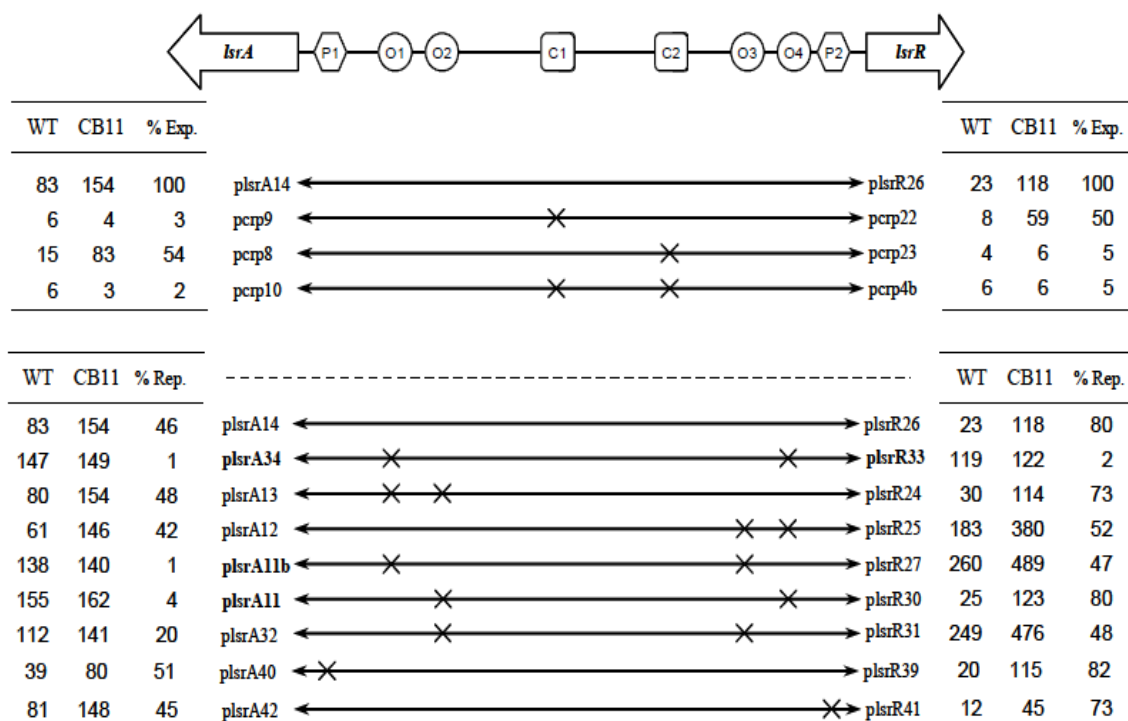
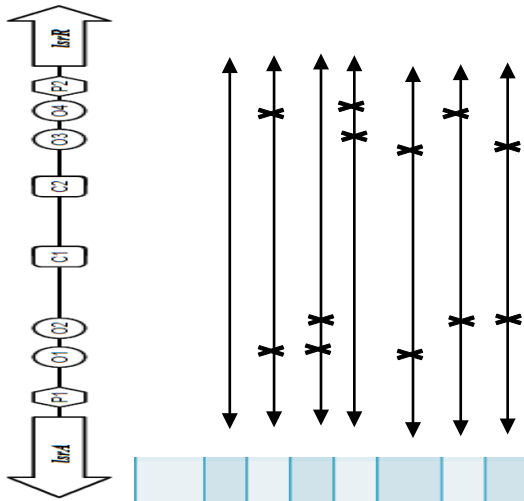


Figure 20: Table of mutations studied in this thesis. Values in this data set are beta-galactosidase activity values taken from measur Modified from [59,76]

Figure 21: Table of plasmids containing the mutations studied in this thesis

Plasmid ID (expressed in lsrA direction)	Plasmid ID (expressed in lsrR direction)	Description of plasmid (excluding promoter and <i>lacZ</i> reporter)	Parameter estimated
plsrA14	plsrR26	Native <i>lsr</i> intergenic region	$K_{bind lsrR}$ & $K_{bind lsrA}$ $V_m lsrR$ & $V_m lsrA$
plsrA34	plsrR33	Contains mutations to putative binding sites O1 & O4	$K_{bind lsrR}$ & $K_{bind lsrA}$
plsrA13	plsrR24	Contains mutations to putative binding sites O1 & O2	$K_{bind lsrR}$ & $K_{bind lsrA}$
plsrA12	plsrR25	Contains mutations to putative binding sites O3 & O4	$K_{bind lsrR}$ & $K_{bind lsrA}$
plsrA11b	plsrR27	Contains mutations to putative binding sites O1 & O3	$K_{bind lsrR}$ & $K_{bind lsrA}$
plsrA11	plsrR30	Contains mutations to putative binding sites O2 & O4	$K_{bind lsrR}$ & $K_{bind lsrA}$
plsrA32	plsrR31	Contains mutations to putative binding sites O2 & O3	$K_{bind lsrR}$ & $K_{bind lsrA}$
plsrA40	plsrR39	Contains mutations to promoter binding site P1	$V_m lsrR$ & $V_m lsrA$
plsrA42	plsrR41	Contains mutations to promoter binding site P2	$V_m lsrR$ & $V_m lsrA$
pcrp9	pcrp22	Contains a mutation to CRP binding site C1	k_{C1} & k_{C2}
pcrp8	pcrp23	Contains a mutation to CRP binding site C2	k_{C1} & k_{C2}

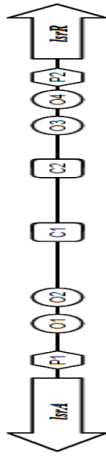
When Byrd ran each mutation in CB11 and Wild Type *E. coli* K12 strains, he reported the expression in terms of Miller Units (as we have used for our model). However, in this experiment, these experiments were run as overnight culture (defined here as $t = 10$ hours) with only the final expression values being reported. We estimate what each mutation does in our system by first estimating our transcription constants— k_{tcR} and B —such that the activity value in our simulation is within 0.1 Miller Units of the experimental value, with a shooting method algorithm described (as a sample global algorithm) in Figure 25 and in detail in Figure 26.



WT (EXP)	CB11 (EXP)	%Rep (EXP)	%Rep (Sim*)	WT (Sim)	CB11 (sim)	B	$K_{\text{resid}} \text{lsrA} \text{ (EM)}$
83	154	46.10	46.06	83.02	153.9	1.305	5.73×10^{-5}
147	149	1.34	10.98	132.67	149.05	1.222	1000
80	154	48.05	48.04	79.99	153.96	1.4	6.66×10^{-5}
61	146	58.22	58.21	60.98	145.92	0.384	7.54
138	140	1.43	9.83	126.23	140.01	0.2863	1000
155	162	4.32	9.99	145.79	161.96	1.317	1000
112	141	20.57	20.55	112.00	140.98	0.2962	72.4

Figure 22: Table of results from simulations involving *lsrA*-directed mutants

Briefly, we selected an initial range of k_{tcR} , and integrated our CB11 model with k_{tcR} in that range. Then, we extracted the $t=600$ point, calculated the beta-galactosidase activity in the lsrR direction, and then calculated the error for each constant relative to the target value. If we were not already within our threshold of 0.1 MU, we looked for a sign change in the error. We selected our new bounds at the sign change, and repeated these steps until we either found a k_{tcR} within our error threshold, or we were approaching some asymptote in the minimum. Having our k_{tcR} , using the CB11 conditions again (since k_{tcR} and B in this case represent transcription without any sort of repression), we used this algorithm to estimate B .



WT (EXP)	CB11 (EXP)	%Rep (EXP)	WT (Sim)	CB11 (sim)	k_{cat} (min ⁻¹)	$K_{m,cat}$ $lsrR$ (μM)
23	118	80.51	22.91	117.95	0.938	3.80×10^{-5}
119	122	2.45	108.95	121.97	0.970	1000
30	114	73.68	30.03	114.05	0.907	5.20×10^{-5}
183	380	51.84	182.99	380.00	3.022	0.0109
260	489	46.83	259.97	489.03	3.889	0.0135
25	123	79.67	25.00	122.98	0.978	4.03×10^{-5}
249	476	47.68	249.03	475.95	3.785	16.4

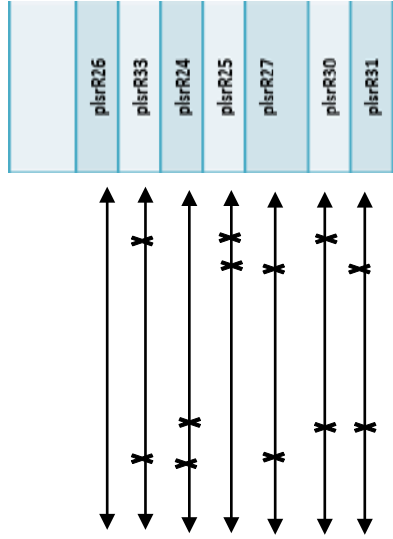



Figure 23: Table of results from simulations involving *lsrR*-directed mutants



B	$K_{\text{bind}} \text{IsrA}$ (μM)	plsrA ID		plsrR ID	k_{ter} (min^{-1})	$K_{\text{bind}} \text{IsrR}$ (μM)
1.305	5.73×10^{-5}	plsrA14	↔	plsrR26	0.938	3.80×10^{-5}
1.222	1000	plsrA34	↔	plsrR33	0.970	1000
1.4	6.66×10^{-5}	plsrA13	↔	plsrR24	0.907	5.30×10^{-5}
0.384	7.54	plsrA12	↔	plsrR25	3.022	0.0109
0.2863	1000	plsrA11b	↔	plsrR27	3.889	0.0135
1.317	1000	plsrA11	↔	plsrR30	0.978	4.03×10^{-5}
0.2962	72.4	plsrA32	↔	plsrR31	3.785	16.4

Figure 24: Binding and constants for each mutation experiment

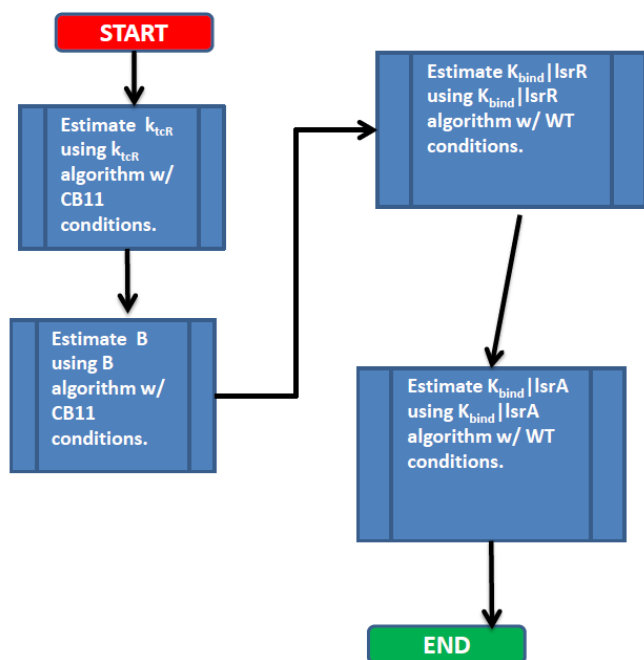


Figure 25. General algorithm used for each mutagenesis experiment. The general algorithm used to estimate each data point in Figures 22-24 as a series of subroutines based on the one shown in Figure 26.

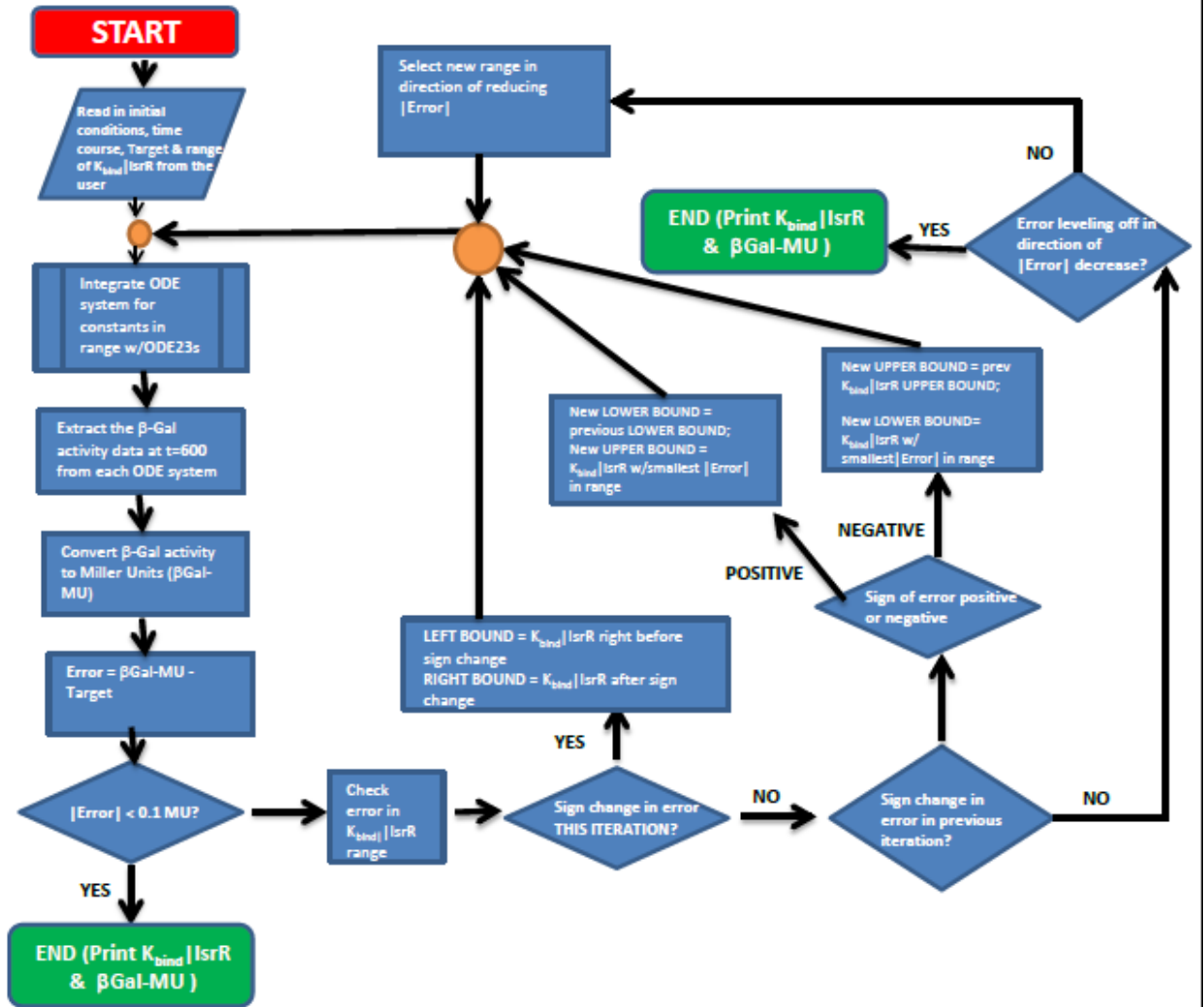


Figure 26: Representative shooting-based algorithm used to estimate $K_{bind}|lslR$ and $K_{bind}|lslA$ in mutation experiments.

In our studies of putative binding site mutations, once we had our k_{icR} and B for each case, switching to the wild type conditions, $K_{bind}|lslR$ and then $K_{bind}|lslA$ were estimated to our error thresholds, except for cases in italics using the algorithm in Figure 22. In those cases, $K_{bind}|lslR$ and $K_{bind}|lslA$ are estimated to a steady-state value. To compare what our activities represented in terms of repression, we calculated percent repression (%Rep) using equation 30, where $\beta Gal|lslX$ represents the beta-galactosidase activity in the $lslX$ direction (in absence of a gene known as

lsrX, we use *lsrX* to represent either the *lsrR* direction or the *lsrA* direction. 100% repression represents 0% expression relative to the *lsrR* knockout. 0% repression indicates that expression levels are very similar to those of the *lsrR* knockout.

$$\%Rep = 100\% \times \left(1 - \frac{\beta_{Gal}|lsrX(Wild\ Type)}}{\beta_{Gal}|lsrX(CB11)} \right) \quad (30)$$

As shown in Figures 23-25, we are able to estimate $K_{bind}|lsrR$ and $K_{bind}|lsrA$ when our system is more than 10% repressed. Under 10% repression, we are only able to hit the ‘steady state’ value. This ‘steady state’ value was determined by doing one iteration of the $K_{bind}|lsrR/K_{bind}|lsrA$ algorithm (see Figure 25) varying $K_{bind}|lsrR$ and $K_{bind}|lsrA$ in the direction which reduces the magnitude of the error in beta-galactosidase activity. These cases feature a mutation at putative binding sites O1, O4, or both. Byrd suggested that these mutations would have a much greater effect than mutations at sites O2 or O3, or both because of the mutations’ proximity to the promoter regions P1 and P2 in the *lsr* intergenic region. In his case, % repression was reduced to <5%. In our case, the O1/O4 mutation resulted in our lowest percent repressions, but no smaller than 9.8% repression in the *lsrR* direction and no smaller than 11% repression in the *lsrA* direction.

Outside of those mutations, our estimation algorithms and our model are able to predict mutant behavior in the putative binding site regions. This model is the first ODE -based model to measure the effects of particular putative binding site mutations . There also appears a dependence of the putative binding site constants on overall transcription of *lsrRK* and *lsrACDB*. Fittingly, in the wild type system, the more *lsrR* mRNA is produced, the more dimer is produced. Because the total amount of binding sites is limited by both our copy number N and our assumption that bacterial population does not change, there are fewer binding sites available for these dimers.

Therefore, the micro-dissociation constants governing these binding reactions will be larger. The larger micro-dissociation constants suggest that a higher concentration of LsrR dimer competition could make the repression step appear weaker. It also compounds a problem of the model as to what happens with excess LsrR dimer. Lu and colleagues found that each LsrR dimer had a distinct ligand-binding domain (LBD) at the C-terminus and a distinct DNA-binding domain at the N-terminus (the opposite end of the protein [73,77]). Although no work has been directly done to study the particular LBD of the LsrR dimers, proteases could recognize and bind to the LBD to degrade the excess dimer. Likewise, we could implement such a degradation model in Michaelis-Menten form, if the kinematics of the degradation reaction of a protease with the matching LBD is known or experimentally determined, or as general protein degradation if not.

Chapter 4: Preliminary Conclusions

In this study, we designed and tested a network ODE-based mathematical model of the dynamics of the *lsr* operon—the “quorum sensing switch” in the AI-2 quorum sensing system in many bacteria. For the first time in *E. coli*, we were able to model the *lsr* operon in its quorum sensing role taking into account the molecular dynamics of LsrR as a tetramer. (Previous models had only considered LsrR as a single repressor, and did not take into account its dynamics, nor those of the *lsr* intergenic region. [43,82]) We also fitted this model to reflect dynamic expression on both sides of the *lsr* operon in response to a dynamic AI-2 profile. We also studied how our binding and transcription constants would change the expression of the operon in either the *lsrR* direction or the *lsrA* direction. The change in expression of genes in the operon, as we note later, may be a proxy for the 140 genes whose expression is altered by knocking down *lsrR*, and by our work and suggestions from the work by Ha and colleagues, changing the ability of LsrR to bind to its binding sites in the *lsr* intergenic region. Byrd inserted plasmids with expression vectors expressed in the *lsrR* direction and the *lsrA* direction containing several mutations of the putative binding sites, whose sequences he identified (reprinted in Figure 27).

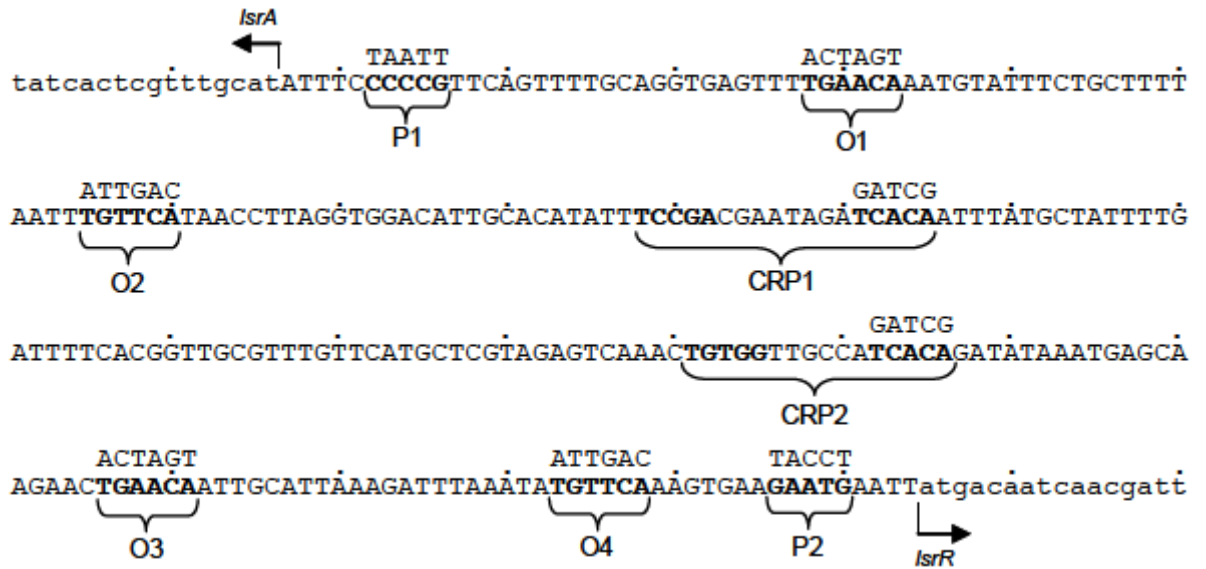


Figure 27: Single strand genetic sequence (with mutations in complement) of the *lsr* intergenic region. [59]

The putative binding site O1 (sequence TGAACA) and putative binding site O3 (sequence TGAACA) are identical. The mutation performed to the complements of both binding sites (4: T→A) is also identical, changing a pyrimidine complement for a purine bonded by the same number of hydrogen bonds. Yet both have different effects. Mutating O1 in conjunction with O4 (TGTTCA: 4: A→G & 5: G→A) decreases %Rep significantly in both *lsrR* and *lsrA* directions, and significantly increases $K_{bind}|lsrR$ and $K_{bind}|lsrA$. But the O1 mutation in any other context seems to be dependent on other mutations. Mutating the seemingly identical O3 site with the same mutation increases k_{tcR} from the 0.9-1 min⁻¹ to 3-5 min⁻¹ range and decreases B from 1.222-1.4 to < 0.38, changing the transcription bias from slightly in the *lsrA* direction to significantly in the *lsrR* direction. The putative binding site constants (micro-dissociation constants) also increase significantly from a base value in the 10⁻⁵ μM range to the 10⁻² μM range. In this context, the single pyrimidine to purine

mutation in O3 may be more significant. It does not simply just pull the DNA base pairing too close for hydrogen bonds to form (and for the DNA) to be stable, but it also significantly decreases the interaction strength between the DBD of the LsrR dimer and O3. Wu and colleagues suggest that the LsrR ligands that might be a part of the DNA binding domain are Gln-33 (glutamine-33), and Tyr-26 (tyrosine-26). Given their codon sequences, it is more likely that the mutation affects the binding of Gln-33 to the putative binding site, and that LsrR binds to O3 at the glutamine-receptive region. Changing the sequence may affect the protein's ability to bind to that residue changing the steric forces between the mutant complement and the normal binding strand. But from Wu's work and comparative studies with the sorbitol operon regulator SorC and the central glycolytic genes regulator (CggR) in *Bacillus subtilis* [83]—two proteins in the SorC DeoR family that are homologous (similar) in structure and function to LsrR, it appears that the steric effects may affect the cooperativity between the dimer.

In cooperative binding, binding of one ligand usually makes the binding of other ligands to the same protein more energetically stable. In DNA-protein interactions there may be an order to the interactions, if the protein ligand binds to multiple DNA sites. In our case, because the O3 mutation has such a strong effect on the transcriptional rates and biases in our simulation, we think that the cooperative binding of LsrR dimer to the *lsr* operon at the putative binding sites O1 and O2, and O3 and O4 might have ordered priority, with the LsrR dimer binding to sites O3 and O4 (*lsrR* direction) having the highest priority.

The phenomenon of “ordered cooperativity” of the system may not be natural to cooperative binding systems, where a ligand can bind to any unsaturated binding site. This may imply that a secondary layer of regulation might be influencing the normal randomness of cooperative binding interactions between our ligand (LsrR dimers) and our receptor (the putative binding half-sites O3 and O4). Our simulations confirm Byrd’s observations that O3 mutations reverse the transcriptional bias of the *lsr* operon, and translate these experimental outputs into computationally relevant kinetic parameters that can reflect more than simply the detectable output of the system. Byrd had initially suggested that there might have existed an integration host factor (IHF) that might specifically recognize the binding half-site O3. IHFs are global gene regulators that have been postulated to have a role in the bending of DNA [84-87] into different forms. Depending on the series of genes IHF binds to, IHF might influence bacterial phenotypes ranging from regulating genes involved with bacterial pathogenicity [88] to the growth of flagella in enterohemorrhagic *E. coli* (EHEC) [85], and may function in gene regulation similar to the role histones play in eukaryotic genetic regulation [89-91]. We suggest that if the O3 binding half-site contains an interaction point for IHF to influence regulation of the *lsr* operon, its effects can be quantified in kinetic terms by our model.

This additional layer of regulation that might surround binding site O3 suggests that the simplistic notion of LsrR as the main quorum sensing “switch” might have a small complication. Our mathematical model reflects the potential for this small complication, and, as previously discussed, translates these complications into kinetic terms. These kinetic terms become much more useful when the output of

our system is no longer simply the expression of *lacZ* (more specifically *lacZYA*), but rather one of 146 genes in *E. coli* alone responsible for auto-aggregation into biofilms, biofilm matrix proteins [80] and invasiveness of *S. typhimurium* [92]. In this context, our simulation work of the *lsr* intergenic region (and LsrR) as the quorum sensing switch provides a simulation framework with which we may not need an experimentally-relevant reporter like *lacZ* to reverse engineer a mechanism for biofilm formation involving the *lsr* quorum sensing system as one part of solving the problem of multiple antibiotic resistant infections (and device contaminations). Although the proliferation of efflux pumps may present another way to mediate MDR directly, no studies have linked any of these efflux pumps, including AcrB in our model system (*E. coli*) to *lsrR*. And thus, the role of LsrR in MDR might be limited to its roles in biofilm formation in *E. coli*.

The series of simulations we performed to test our model of the *lsr* quorum sensing system may thus be used to study MDR in the context of biofilm formation. While we discuss a very basic future applications of this first-principles mode in Section 5, these applications can be tied into MDR by providing a simple method with which we can assess the presence, quantity, and function of biofilm building blocks from bacteria utilizing the *lsr* quorum sensing system that has been shown, in biofilms involving other bacterial species besides *E. coli*, to increase MDR 1000-fold[93]. Other models of the *lsr* quorum sensing system developed by Hooshangi and Bentley [43] and Gonzalez Barrios and Achenie [82] address the overall *lsr* quorum sensing system without considering the dynamics of the LsrR quorum sensing “switch” that affects so many genes involved with biofilm formation and thus

MDR. Our model incorporates kinetic details of the expression of LsrR, its several forms, and tie in the dynamics of those forms of LsrR to an output which can be converted to a framework to monitor the kinetics of the *lsrR*-linked proteins that may form the building blocks to one form of MDR. Our parameter search studies also present a method by which future modelers can perform virtual mutagenesis experiments on ODE systems with a genetic component to estimate changes on an MDR protein or gene of interest. And combining with our use of experimental units that can be measured by standard experimental assays, rather than bulk concentration measurements, our model presents a platform on which experimenters can predict the behavior of network components in their model system that may be accessible via experimentation, and allow them to gain more systemic relevance from their experiments. No other model of the *lsr* quorum sensing system has been able to offer such convenience and modeling opportunity to experimenters. And so, besides being able to translate the findings of Byrd into a simulation-based context (and providing evidence for Gln-33 being the primary binding residue in LsrR to O3 and O1), we have done so in a way that experimenters can integrate their own population dynamics and *lsr*-dependent activity assays (of any kind).

Chapter 5: Future Work

The model we developed provides a preliminary indication of how LsrR quorum sensing might work when we fill in the details of the molecular structures and interactions of the many proteins involved in autoinducer-2 quorum sensing systems, and in particular, Lsr-based AI-2 quorum systems. We demonstrated our ability to model how altering the dynamics of *lsr* binding regions, as well as the polymeric forms of the repressor LsrR might affect expression of genes on either side of the *lsr* operon. However, this work provides a foundation later research that we would like to do. This section addresses several of those concerns.

Section 1: cAMP-CRP Binding Interactions

One complication we had in constructing our model was our limited knowledge of the CRP interactions in our system. Early studies suggest that CRP-binding interactions not just implicate cAMP-CRP binding in upregulating or downregulating transcription of genes on either side of the *lsr* operon [59,94], but they might also be implicated in the folding and unfolding of the *lsr* operon. Data shown in Figure 19, showing the effects of CRP binding site mutations and our simulations reflecting the mutations in Figure 26 are shown in Figures 27 and 28, reflect the possible effects of mutating the different combinations of CRP binding site knockout mutations on expression of the intergenic region. In these cases, we utilized CB11 (*lsrR* knockout strains) whose basal transcription characteristics were similar to those *E. coli* strains containing the *plsrR26* & *plsrA14* plasmids ($k_{\text{tCR}} = 0.938 \text{ min}^{-1}$

and $B = 1.305$). With our putative binding site constants ($K_{bind}|lsrR$ and $K_{bind}|lsrA$) and our promoter binding site constants ($V_m|lsrR$ and $V_m|lsrA$) set to their base values, we estimate our CRP-binding constants k_{C1} and k_{C2} using a similar algorithm to what we had used to estimate $K_{bind}|lsrR$ and $K_{bind}|lsrA$.

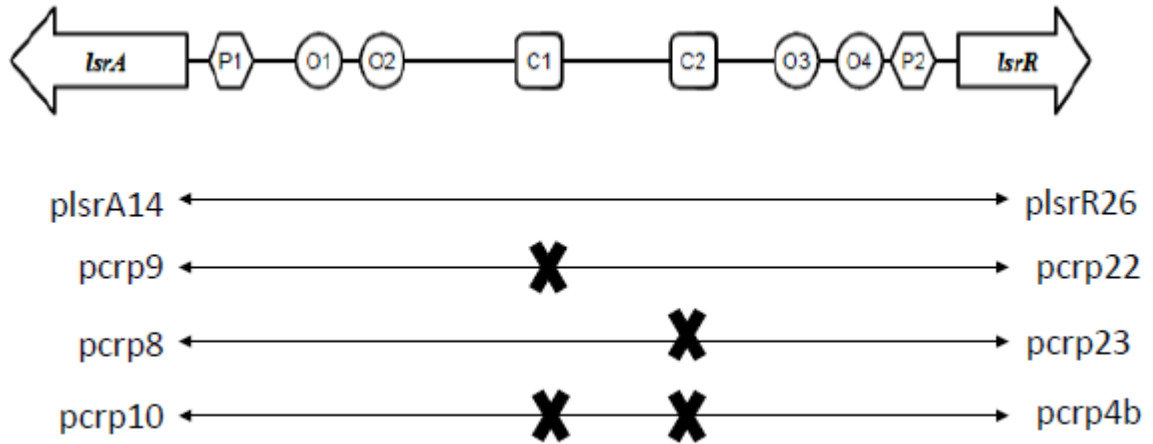


Figure 28: Graphical representation of CRP binding site mutations, taken and modified from [59]. Xs represent the sites in the *lsr* intergenic region were mutated.

WT (EXP)	CB11 (EXP)	%Expr (EXP)	%Expr (Sim*)	CB11 (Sim)	K_{d1} ($\mu M^{-1} min^{-1}$)	
83	154	100	100	153.9	1	plsR26
6	4	2.59	2.55	3.93	0.022	pcrp22
15	83	53.89	53.87	82.93	0.486	Pcrp23
6	3	1.95	1.90	2.92	0.016	pcrp4b

Figure 29: Simulation results of mutation experiments expressed in the *lsrA* direction.

WT (EXP)	CB11 (EXP)	%Expr (EXP)	%Expr (Sim*)	CB11 (Sim)	K_{d1} ($\mu M^{-1} min^{-1}$)	
23	118	100	100	118.0	1	plsR26
8	59	50	50.0	58.98	0.468	pcrp22
4	6	5.08	5.09	6.00	0.045	Pcrp23
6	6	5.08	5.09	6.00	0.045	pcrp4b

Figure 30: Simulation results of mutation experiments expressed in the *lsrR* direction

Our early simulation results suggest that we can reflect changes in the CRP binding sites in the expression of both sides of the *lsr* operon, and that there appears to be no limit on how low our percent expression (%Exp), defined in Equation 31, can go (with 100% expression representing the expression of our positive control (plsrA14 & plsrR26)).

$$\%Exp = 100\% \times \left(\frac{Exp(perpK)}{Exp(Positive\ control)} \right) \quad (31)$$

This model still does not account for CRP assisting the folding of the *lsr* operon, as a step in reforming the LsrR tetramer in the absence of AI-2. Nor does it necessarily involve for any potential integration factors [59,76] that might interact with the *lsr* intergenic region that might assist the DNA in reforming the hairpin loop structure. Our work will move towards explaining and modeling the factors necessary in order to model this looping process.

Section 2: Promoter Binding Sequences

Some of our real mutation experiments have also included simulating what happens when a mutation occurs not within a putative binding site or CRP binding site, but within a promoter binding site. There are two promoter regions that promoters can bind to in order to enhance transcription of the *lsr* operon—sites P1 and P2 shown in Figure 19, which sit close to the *lsrR* and *lsrK* and *lsrACDB* genes in the *lsr* operon[59,76]. Since we assumed that a mutation to either promoter region might have an influence on expression of the *lsr* operon in both directions, we incorporated this into our model. Rather than having the promoter site mutation directly affect transcription and thus the bidirectional expression of the *lsr* operon, we implemented

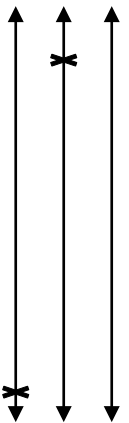
the promoter changes through the constants $V_m|l\text{srR}$ and $V_m|l\text{srA}$, the maximum reaction rates of the repression step. If the mutation of the promoter binding site downregulates expression in either direction relative to the positive control (p $l\text{srA14}$ & p $l\text{srR26}$), the mutation is said to increase $V_m|l\text{srR}$ or $V_m|l\text{srA}$. If the promoter binding site mutation turns out to upregulate expression in the same direction ($l\text{srR}$ or $l\text{srA}$) relative to the positive control, then $V_m|l\text{srR}$ or $V_m|l\text{srA}$ decreases relative to the positive control value. Experimental results, as well as our simulation results initially mentioned in Figure 19 and summarized in Figures 29 and 30 suggest that $V_m|l\text{srR}$ and $V_m|l\text{srA}$ do not change in a way that is necessarily consistent, nor is the change in expression in the $l\text{srR}$ or $l\text{srA}$ directions very significant. The sequence of the promoter sequence is known, but a clearer picture of other secondary promoters and regulators that might affect how the promoter might be expressed is not known, and represent a category of simulations that we might want to carry out in the future.

WT (EXP)	CB11 (EXP)	%Rep (EXP)	%Rep (Sim*)	WT (Sim)	CB11 (sim)	B	V _{max} (uM/min)
83	154	46.10	46.09	82.98	153.942	1.305	2.14
39	80	51.25	51.21	39.01	51.21	0.695	3.37
81	148	45.27	45.30	80.97	148.02	3.288	3.62

plsrA14
plsrA40
plsrA42



Figure 31: Simulation results of promoter-site mutations in the *lsr* intergenic region in the *lsrA* direction. These reflecting these effects by modifying $V_m|_{lsrA}$. Simulations were carried out using an algorithm similar to those for determining $K_{bind}|_{lsrA}$ for putative binding site experiments.



	WT (Exp)	CB11 (Exp)	%Rep (Exp)	%Rep (Sim*)	WT (Sim)	CB11 (sim)	k_{cat} (min^{-1})	V_{max} lsrR ($\mu\text{M}/\text{min}$)
plsR26	23	118	80.50	80.49	23.01	117.95	0.983	3.73
plsR39	20	115	82.60	82.61	20.01	115.06	0.915	4.45
plsR41	12	45	73.33	73.26	12.03	45.02	0.358	3.70

Figure 32: Simulation results of mutation experiments involving promoter-site mutations in the *lsrR* direction. These mutations were reflected by by modifying $V_m|lsrR$. Simulations were carried out using an algorithm similar to those for determining $K_{bind}|lsrR$ for putative binding site experiments.

Section 3: Other modifications to the Model

The model we developed offers a simplistic insight into how the structure and details of the LsrR repressor may affect the expression of genes on both sides of the *lsr* operon. It is simplistic because we made several assumptions that took out the complexities of AI-2 synthesis, potential interactions with other autoinducers, as well as AI-2 importation and AI-2 phosphorylation. Below we detail several changes to the model that we will make for future studies.

Subsection 1: Incorporating AI-2 Importation and LsrK Dynamics

In real Lsr-based quorum systems, AI-2 is imported using an active form of Lsr, which we have shown to be synthesized. In the real system, we might expect a positive-feedback loop of AI-2 importation and phosphorylation by LsrK leads to the synthesis of more Lsr importers, and thus more AI-2 is imported, etc. until the system runs out of AI-2. In reality LsrK would not necessarily be the first importer. Some studies have identified the phosphoenolpyruvate (PEP)-transferase system (PTS) as the initial importer of AI-2 when quorum sensing conditions have been met (AI-2 concentration above one threshold, bacterial density above another threshold) [66]. We will detail the dynamics of the PTS / alternative pathway in internalizing and processing AI-2, and the production of LsrK as a protein product in our system. However, it is unclear how much of a role the PTS pathway plays once LsrK is in the system. These modeling experiments may help to elucidate the role and timing of both the PTS pathway, and the LsrK pathway. And in the case of LsrK, we may also be able to test out different inhibitors of the system.

Subsection 2: Incorporating AI-2 Synthesis

As previously mentioned in this work, we removed AI-2 synthesis from the equation, and simply forced AI-2 curve based on data tracking AI-2 levels in *E. coli* samples, and assumed AI-2 was synthesized elsewhere, and intracellular and extracellular AI-2 were in equilibrium with each other, and that the AI-2 concentration (or population) threshold typically required for bacteria, including *E. coli*, to exhibit population-dependent behavior was already met. The AI-2 synthetic pathway is one that is widely conserved and well-elucidated in *E. coli* [59,76,77,79] and other bacterial species [95-100]. We plan on incorporating the synthetic pathway in future models. There are several ways we could do this. One way could be to simply implement the AI-2 synthetic pathway. But that would also incorporate a complication of auto-importation (a cell utilizing AI-2 it had just produced) that we could set some basic conditions and determine how auto-importation complicates matters. It might be a way to explain why Luo and colleagues separated AI-2 synthesizers from AI-2 receivers in his AI-2-based microfluidics device [69]. Current literature seems to only suggest or implicate the protein TqsA as a chief exporter of AI-2. And because AI-2 itself is relatively conserved, there may not be a limit as to how much specificity each AI-2 molecule could have. Providing an answer on auto-importation could help determine whether it is something we need to worry about as we expand our model.

Subsection 3: Incorporating Our Model Into a Population-Based Model

While we model quorum-sensing using a constant population, quorum sensing in itself is a population-dependent behavior. More often than just cells synthesizing lots of AI-2 before importing it back in, quorum sensing mediates responses of groups of cells to environmental conditions and mediates a response to those conditions. This could mean that, instead of simply mediating the response by the expression of reporters of activity of the *lsr* operon, the output of our model could be the synthesis of biofilms, the actuation of antibiotic resistance mechanisms, or swimming in the direction of the AI-2—outputs that cannot necessarily be measured by the standard beta galactosidase activity assay.

In future work, we have several different means of incorporating population dynamics into our model. Most simply, we could tie our OD₆₀₀ that we used to calculate Miller Units from bulk concentration to the population of bacteria in some test volume. The supplemental text in Section 6.2 (Chapter 6, Section 2) provides a preliminary method of how we tied OD₆₀₀ into our calculation, but in the case of our model case we assumed an OD₆₀₀ of 1.0 throughout the entire length of our simulation (and in all the simulation data presented in this work). But any vector of OD₆₀₀ data can be used here. And thus, we can tie our model implicitly to population growth or death based on definition of the Miller Unit alone.

To add more complication, we could tie AI-2 synthesis and protein and small nucleotide synthesis to population growth. We could implement this simply using a Monod model of bacterial growth and substrate consumption, and simply imply substrates are consumed in the synthesis of key molecules like AI-2, cyclic AMP,

ATP, and the *lsr* operon. But that leaves the question of how substrates are reformed, because eventually the cultural substrate might run out.

Subsection 4: Simulating the Effects of Inhibitors

Many efforts have been in place to examine possible quorum sensing inhibitors. Much has been made by the use of AI-2 inhibitors and some studies, AI-2 analogs which can be phosphorylated by LsrK, but cannot de-repress the *lsr* operon. These drugs, which are collectively known as quorum sensing inhibitors (QSIs), show promise in treating MDR [60,61]. Our model offers a way in which we could reflect the effects of these drugs on expression of both sides of the *lsr* operon, and downstream genes that could convey MDR.

One such class of drugs may be AI-2 analogs—molecules that are structurally similar to AI-2 to bind LsrK [101], but not similar enough to AI-2 to de-repress the *lsr* operon. These molecules could contain the basic DPD structure, but they may contain alkyl functional groups (ethyl, propyl, butyl, hexyl) whose hydrophobic interactions may not align well with the LBD of LsrR [102], because DPD may not cyclize into R/S-DHMF a secondary precursor that must be further hydrated and modified in order to form AI-2. With these, so far *in vitro*, propyl-DPD has demonstrated to be an antagonist of the quorum sensing circuit—but it lowers the effective k_{cat} from 7.6 s^{-1} (432 min^{-1}) to 5.8 s^{-1} (348 min^{-1}), and the effective K_m is increased from 1.0 mM ($1000 \text{ }\mu\text{M}$) to 1.4 mM ($1400 \text{ }\mu\text{M}$) [101]. However, IC_{50} , which is related to K_i (the inhibition constant for the phosphorylation of DPD (AI-2)) is $5.3 \text{ }\mu\text{M}$, which is within the range of our simulation. The form of IC_{50} used also

implies that propyl-DPD (and other AI-2 analogues) may be competitive inhibitors, though this observation has yet to be tested. This seems to suggest that propyl-DPD might be a very effective QS inhibitor, which we could represent in our model as a competitive inhibitor to DPD binding to LsrK.

Subsection 5: Algorithm Changes

Even just keeping our model as is, we would like to apply several changes to our algorithm to make our estimation algorithm more robust.

One way, or investigation that we may need to do is reverse the order of $K_{\text{bind}}|\text{lSrR}$ and $K_{\text{bind}}|\text{lSrA}$ calculations. Preliminary results (not shown here) suggest that the magnitude of our binding constants do not change because which binding constant to calculate first. But this needs to be extended to each experiment to confirm these initial findings.

One other change may be to fit our model—both in the lsrR direction and the lsrA direction (transcription and binding as well) in the same window. In our model, we estimated k_{tcR} , B , $K_{\text{bind}}|\text{lSrR}$, and $K_{\text{bind}}|\text{lSrA}$ in separate directories (though all under the same directory). With ODE23s, the exact value of the output changes with each iteration. While the variations are generally <10 Miller Units in this work, it may be significant enough that it could throw off $K_{\text{bind}}|\text{lSrR}$ and $K_{\text{bind}}|\text{lSrA}$, as well as B . Our future work, with this modification, may help us determine how different our estimations were, and whether our observations from this study hold up with ODE23S actually holding the beta-galactosidase activities constant. Early prototypes geared at automating this process have proven to be computational inefficient in the MATLAB language—we see enough that it is possible to streamline our algorithm without switching languages/development environments or integrators.

Chapter 6: Supplementary Material

Supplementary Figure 1: Equations used in our model

Equation #	ODE	Module
I ((2) in text)	$\frac{dA_o}{dt} = -2 \left(\frac{\alpha(t - \beta)}{\gamma} \right) e^{-\left(\frac{t - \beta}{\gamma}\right)^2}$	Importation
II	$\frac{dATP}{dt} = -ATP (k_{lsrK}A_o + k_{deg} - (k_{lsrK}A_o + k_{deg})) = 0$	AI-2 Processing
III	$\frac{dADP}{dt} = k_{lsrK}A_oATP - k_{deg}ADP$	AI-2 Processing
IV	$\frac{dA_p}{dt} = k_{lsrK}A_oATP - (k_{bind}A_p^2T_b + k_{deg Ap}A_p)$	AI-2 Processing
V	$\frac{dT_b}{dt} = k_{tet}D_{b lsrA}D_{b lsrR} - k_{bind}A_p^2T_b$	Quorum Sensing Actuation
VI	$\frac{dD_{p lsrR}}{dt} = k_{bind}A_p^2T_b - k_{cleave_1}D_{p lsrR}$	Quorum Sensing Actuation
VII	$\frac{dD_{p lsrA}}{dt} = k_{bind}A_p^2T_b - k_{cleave_2}D_{p lsrA}$	Quorum Sensing Actuation

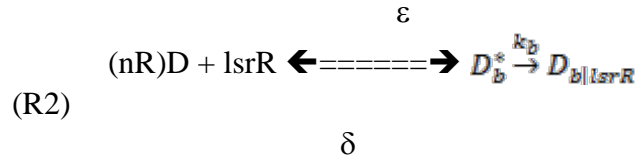
VIII	$\frac{dD_p}{dt} = k_{\text{cleave}_1} D_{p_b lsrR} + k_{\text{cleave}_2} D_{p_b lsrA} - k_{\text{deg} D_p} D_p$	Quorum Sensing Actuation
IX	$\frac{dlsrR}{dt} = k_{\text{cleave}_1} D_{p_b lsrR} - \frac{V_{m_{lsrR}} D^{nR}}{K_{\text{bind} lsrR}^{nR} + D^{nR}} lsrR$	Quorum Sensing Actuation
X	$\frac{dlsrA}{dt} = k_{\text{cleave}_2} D_{p_b lsrA} - \frac{V_{m_{lsrA}} D^{nA}}{K_{\text{bind} lsrA}^{nA} + D^{nA}} lsrA$	Quorum Sensing Actuation
XI	$\frac{d(mRNA lsrR)}{dt} = k_{\text{tcR}} \left(\frac{cAMP; CRP; C1}{C1} \right) lsrR - k_{\text{deg} mRNA} (mRNA lsrR)$	Quorum Sensing Actuation
XII	$\frac{d(mRNA lsrA)}{dt} = k_{\text{tcA}} \left(\frac{cAMP; CRP; C2}{C2} \right) lsrA - k_{\text{deg} mRNA} (mRNA lsrA)$	Quorum Sensing Actuation
XIII	$\frac{d(mRNA X)}{dt} = k_{\text{tcR}} \left(\frac{cAMP; CRP; C1}{C1} \right) lsrR - k_{\text{deg} mRNA} (mRNA X)$	Quorum Sensing Actuation

XIV	$\frac{d(mRNA Z)}{dt} = k_{tclA} \left(\frac{cAMP, CRP, C2}{C} \right) IsrA - k_{deg_mRNA} (mRNA Z)$	Quorum Sensing Actuation
XV	$\frac{d(\beta Gal IsrR)}{dt} = k_{tl}(mRNA X) - k_{deg \beta Gal}(\beta Gal IsrR)$	Quorum Sensing Actuation
XVI	$\frac{d(\beta Gal IsrA)}{dt} = k_{tlA}(mRNA Z) - k_{deg \beta Gal}(\beta Gal IsrA)$	Quorum Sensing Actuation
XVII	$\frac{dA}{dt} = k_{tlA}(mRNA IsrA) - k_{deg}A$	Quorum Sensing Actuation
XVIII	$\frac{dM}{dt} = k_{tl}mRNA IsrR - (k_{pol}M^2 + k_{deg_M}M)$	Quorum Sensing Actuation
XIX	$\frac{dD}{dt} = k_{pol}M^2 - \left[\frac{V_{m IsrR} D^{NR}}{K_{bind IsrR}^{NR} + D^{NR}} IsrR + \frac{V_{m IsrA} D^{NA}}{K_{bind IsrA}^{NA} + D^{NA}} IsrA \right] - k_{deg_D}D$	Quorum Sensing Actuation
XX	$\frac{dD_{b IsrR}}{dt} = \frac{V_{m IsrR} D^{NR}}{K_{bind IsrR}^{NR} + D^{NR}} IsrR - k_{tet}D_{b IsrR}D_{b IsrR}$	Quorum Sensing Actuation
XXI	$\frac{dD_{b IsrA}}{dt} = \frac{V_{m IsrA} D^{NA}}{K_{bind IsrA}^{NA} + D^{NA}} IsrA - k_{tet}D_{b IsrA}D_{b IsrA}$	Quorum Sensing Actuation

XXII	$\frac{d(cAMP)}{dt} = k_{regen}(cAMP:CRP:C1 + cAMP:CRP:C2) - k_{cAMP}(cAMP)(CRP)$	cAMP-CRP
XXIII	$\frac{dCRP}{dt} = k_{regen}(cAMP:CRP:C1 + cAMP:CRP:C2) - k_{cAMP}(cAMP)(CRP)$	cAMP-CRP
XXIV	$\frac{d(cAMP:CRP)}{dt} = k_{cAMP}(cAMP)(CRP) - (k_{c1} + k_{c2})(cAMP:CRP)$	cAMP-CRP
XXV	$\frac{dC1}{dt} = k_{regen}(cAMP:CRP:C1) - k_{c1}(cAMP:CRP)C1$	cAMP-CRP
XXVI	$\frac{dC2}{dt} = k_{regen}(cAMP:CRP:C2) - k_{c1}(cAMP:CRP)C2$	cAMP-CRP
XXVII	$\frac{d(cAMP:CRP:C1)}{dt} = k_{c1}(cAMP:CRP)C1 - k_{regen}(cAMP:CRP:C1)$	cAMP-CRP
XXVIII	$\frac{d(cAMP:CRP:C2)}{dt} = k_{c2}(cAMP:CRP)C2 - k_{regen}(cAMP:CRP:C2)$	cAMP-CRP

Section 1: Cooperative Binding Events

We assume that the binding of our lsrR dimer to its binding sites on either side of the lsrR operon represent the only cooperative binding events in our system. For either case, we assume that our reaction series is defined by reaction R2, where nR is the cooperativity coefficient defined as by table 2, D_b^* is an unstable complex initially formed when the dimer reversibly binds to *lsrR* at binding sites O1 and O2, ϵ and δ are rate constants that govern the forward and reverse reactions at the first step of R2. k_b is the rate constant governing the binding and stabilization of D_b^* to lsrR to form the stable species, $D_{b|lsrR}$ (the dimer irreversibly bound to O1/O2).



We now focus on the reversible step, and assume the forward and reverse reactions reach rapid equilibrium, and write our balance.

$$\epsilon D^{nR} lsrR = \delta D_b^* \quad (3)$$

We also introduce a new constant, K_α^* , our association equilibrium constant, as defined in (4).

$$K_\alpha^* = \frac{\epsilon}{\delta} \quad (4)$$

We solve (3) for D_b^* and utilize our definition in (4) to obtain the expression in (5).

$$D_b^* = \frac{\epsilon}{\delta} D^{nR} lsrR = K_\alpha^* D^{nR} lsrR \quad (5)$$

We now initially consider our second reaction, and write a simple ODE for the formation of $D_{b|lSrR}$ and define this expression as our reaction velocity v in (6), where k_b is defined as in (7).

$$\frac{dD_{b|lSrR}}{dt} = v = k_b lSrR \quad (6)$$

$$k_b = V_{m|lSrR} \theta \quad (7)$$

$V_{m|lSrR}$ is defined in Table 3, and θ is the saturation of our free $lSrR$ molecules as defined in (8).

$$\theta = \frac{D_b^*}{D_b^* + lSrR} \quad (8)$$

We now substitute in the final expression in (5) for D_b^* into (8), and simplify (dividing out the common $lSrR$ term).

$$\theta = \frac{K_d^* D^{nR}}{K_d^* D^{nR} + 1} \quad (9)$$

We now define our dissociation constant, K_D , in (10) and multiply (9) by (10) to obtain our final saturation form in (11).

$$K_D = \frac{1}{K_d^*} \quad (10)$$

$$\theta = \frac{D^{nR}}{D^{nR} + K_d} \quad (11)$$

The expression in (11) represents one form of the Hill equation. However, it may be more important for us to find the dissociation constant at which 50% of the available binding sites are saturated. We can solve for K_d when $\theta = 0.5$. We solve (11) with this substitution to find out that $K_d = D^{nR}$. We select the value for our dimer concentration D (whatever that value K_d could be for our data), and assign it as $K_{b|lSrR}$, obtaining our final expression for θ in (12), and substituting into (7) to obtain our

final expression for our cooperative binding term, k_b . Then, we plug (13) back into (6) to get our final expression for cooperative binding velocity, which is cooperative in relation to our dimer.

$$\theta = \frac{D^{nR}}{D^{nR} + K_b^{nR}} \quad (12)$$

$$k_b = V_{m|lSR} \left(\frac{D^{nR}}{D^{nR} + K_b^{nR}} \right) \quad (13)$$

$$v = \left(\frac{V_{m|lSR} D^{nR}}{D^{nR} + K_b^{nR}} \right) lSR \quad (14)$$

Section 2: Derivation of the Miller Unit-to-Concentration Conversion Factor, κ

In order for a mathematical model to be relevant for experimenters, the model must, in our case, find methods to use the terms and outputs of experimental work. In many quorum sensing experiments, this output is usually tied to a change in visual output, with some quantification of that visual output, whether in Miller Units, *Vibrio* BB170 assays, or fluorescence imaging. Generally speaking, this requires the insertion of a reporter gene, which produces either a fluorophore or a protein that will trigger a color-change response to a standard assay.

For our model, since we are modeling data presented by Byrd et al., we represent our experimental data in Miller Units, which is based on early investigations of the *lac* operon by Jeffery Miller and colleagues[103-105]. Classically, the Miller Unit can be defined as in (15), where A_{420} and A_{600} are absorbances of our bacterial sample at light wavelengths of 420 Hz and 600 Hz, and A_{550} measures the absorbance of scattered light at 420nm, due to cell debris.

$$1 \text{ MU} = \frac{1000 (A_{420} - 1.75A_{550})}{t_{\text{experiment}} V_{\text{sample}} A_{600}} \quad (15)$$

If we assume that cell debris scattering is negligible in comparison to the direct absorption at 420nm, and 600nm, (15) reduces to the form in (16).

$$1 \text{ MU} = \frac{1000 A_{420}}{t_{\text{experiment}} V_{\text{sample}} A_{600}} \quad (16)$$

In order to proceed from here, we could note that A_{600} is dependent on the bacterial population density. In our model, we assume that if we observe an $A_{600} = 1.0$, we have a cell density of $\sim 10^9$ cells/mL. Likewise, we assume our operating volume, V_{sample} is 1.0 mL, we also assume that time (t) is 1 time unit—which will

change if we want to define our Miller Unit in terms of time in seconds, minutes, or hours.

We must also consider our A_{420} . Our model has been developed in terms of bulk concentration μM . But equation (15) and (16) require that we utilize absorbance. The Beer-Lambert law, as shown in (17), defines optical density (absorbance) at a particular wavelength for a known species as linearly proportional to the bulk molar concentration of that species (C). We assume we are carrying out a single spectrophotometric experiment, since our indicator, a product of beta-galactosidase metabolism, produces a chromophore that emits visible light at a single wavelength.

$$A_{\lambda} = E_{\lambda}C \quad (17)$$

In (17), A_{λ} is the optical density (absorbance) of light at a wavelength λ E_{λ} is an extinction coefficient, which we will define here nominally in units of μM^{-1} , and the concentration of beta galactosidase produced from our targeted reporter, in μM .

However, to do our conversion we will need to make a couple further assumptions. First, cells fill the entire 1 mL volume of our test system. Second, we will assume that a single *E. coli* cell has a volume of $\sim 1 \times 10^{-15}$ L.

Before we begin the next step in our conversion process, we must convert a concentration in terms of molecules/cell to μM ($\times 10^{-6}$ mol/L), as shown below, starting off with a concentration of 1 molecule/cell.

$$C_o = 1 \frac{\text{molecules}}{\text{cell}} \left(\frac{1 \text{ mol}}{6 \times 10^{23} \text{ molecules}} \right) \left(\frac{\text{cell}}{1 \times 10^{-15} \text{ L}} \right) \left(\frac{10^6 \mu\text{M}}{1 \text{ mol/L}} \right) = 0.00167 \mu\text{M}$$

The rest of the conversion process is not as straight forward.

While we initially define (16) in terms of our concentration by (17), most beta-galactosidase manufacturers produce synthetic beta galactosidase will rate their beta galactosidase samples by the number of activity units generated per mg beta galactosidase. For our model, we selected a beta galactosidase produced by Sigma Aldrich that has an activity of 600 activity units (AU) per mg protein, which we will define as shown in Supplementary Figure 2.

$$\left(\frac{1 \text{ molc } \beta Gal}{\text{cell}}\right) X V_{\text{cell}} (MW) \left(\frac{1 \text{ mg}}{1000 \mu g}\right) GA_{600} N \left(\frac{1000 \text{ Miller Units}}{1 \text{ Activity Unit}}\right) \left(\frac{1}{X}\right)$$

$$= 75 \frac{\text{Miller Units}}{\mu M \beta Gal}$$

Parameter	Definition	Value	Source/Assumed?
N	Conversion between A_{600} (spectrophotometric absorbance at 600nm) and cell density	1×10^9 cells/mL / (1 A_{600})	Assumed
N_A	Avogadro's number	1 mol = 6×10^{23} molecule(s)	Assumed
G	Activity per mass beta galactosidase protein	600 activity units/mg protein	Sigma-Aldrich, 2013
MW	Molecular wt. beta-galactosidase	125 kDa = 125,000 mg/mmol	Assumed
X	Conversion factor between molecules/ <i>E. coli</i> cell and bulk concentration	1 molecule/cell = 0.00167 μ M	This paper
V_{cell}	Typical volume of <i>E. coli</i> cell	1×10^{-15} mL	Assumed
V_{sample}	Total sample volume	1 mL	Assumed

Supplementary Figure 2: Parameters used in our conversion

Supplementary Figure 3: State variables in this model

Variable	Definition	Type	Initial Value	Source
<i>A</i>	Transporter protein Lsr;	Concentration	0 μM	This paper, Assumed
<i>ADP</i>	Intracellular adenosine diphosphate (ADP)	Concentration	0 μM	This paper, Assumed
<i>A_o</i>	Autoinducer-2 (AI-2) outside our system	Concentration	0.0045 μM	This paper, Assumed
<i>A_p</i>	Phospho-AI2 (AI2-P), intracellular	Concentration	0 μM	This paper, Assumed
<i>ATP</i>	Intracellular adenosine triphosphate (ATP)	Concentration	5 μM	[106] [107]
<i>C1</i>	cAMP binding site on <i>lsrR</i> side of <i>lsr</i> operon	Concentration	20 molecules/cell	This paper, Assumed
<i>C2</i>	cAMP binding site on <i>lsrA</i> side of <i>lsr</i> operon	Concentration	20 molecules/cell	This paper, Assumed
<i>cAMP</i>	Cyclic AMP (cAMP)	Concentration	0.1 μM	This paper, Assumed

<i>cAMP:CRP</i>	Cyclic AMP-CRP complex	Concentration	1300 molecules/cell	[13][107]
<i>cAMP:CRP:C1</i>	cAMP-CRP complex bound to C1	Concentration	0 μM	This paper, Assumed
<i>cAMP:CRP:C2</i>	cAMP-CRP complex bound to C2	Concentration	0 μM	This paper, Assumed
<i>D</i>	lsrR protein, dimer	Concentration	0 μM	This paper, Assumed
<i>D_{b lsrA}</i>	lsrR dimer bound to <i>lsrACDB</i> at O3/O4	Concentration	0 μM	This paper, Assumed
<i>D_{b lsrR}</i>	lsrR dimer bound to <i>lsrRK</i> at O1/O2	Concentration	0 μM	This paper, Assumed
<i>D_p</i>	AI2-P/lsrR dimer complex, free	Concentration	0 μM	This paper, Assumed
<i>D_{p,b lsrA}</i>	AI2-P/lsrR dimer complex, bound to O3/O4; intermediate in tetramer cleavage reaction	Concentration	0 μM	This paper, Assumed
<i>D_{p,b lsrR}</i>	AI2-P/lsrR dimer complex, bound to O1/O2; intermediate in tetramer cleavage reaction	Concentration	0 μM	This paper, Assumed

<i>lsrA</i>	Activated/free <i>lsrACDB</i> gene(s) available for transcription	Concentration	20 molecules/cell	This paper, Assumed
<i>lsrR</i>	Activated/free <i>lsrRK</i> gene(s) available for transcription	Concentration	20 molecules/cell	This paper, Assumed
<i>M</i>	lsrR monomer	Concentration	0 μ M	This paper, Assumed
<i>mRNA lsrA</i>	mRNA transcribing the transporter synthesized from <i>lsrACDB</i>	Concentration	0 μ M	This paper, Assumed

<i>mRNA lsrR</i>	mRNA transcribing monomer synthesized from <i>lsrRK</i> (<i>lsrK</i> knockout)	Concentration	0 μ M	This paper, Assumed
<i>mRNA X</i>	<i>lacZ</i> Reporter mRNA reporting <i>lsrRK</i> transcription	Concentration	0 μ M	This paper, Assumed
<i>mRNA Z</i>	<i>lacZ</i> Reporter mRNA reporting <i>lsrACDB</i> transcription	Concentration	0 μ M	This paper, Assumed
T_b	<i>lsrR</i> tetramer	Concentration	20 molecules/cell	This paper, Assumed
<i>βGal lsrA</i>	β -Galactosidase activity associated with synthesis of transporter	Activity	0 Miller Units	This paper, Assumed
<i>βGal lsrR</i>	β -Galactosidase activity associated with synthesis of <i>lsrR</i> monomer	Activity	0 Miller Units	This paper, Assumed

Parameter	Definition	Base Value/Units	Source
B	Bias to transcribe towards <i>lsrACDB</i> side of <i>lsr</i> operon	1.225 (unitless)	This thesis, fitted to Fig 3.6 from [59]
$K_{bind lsrA}$	Michaelis-Menten constant governing the cooperative binding of the <i>lsrR</i> dimer to binding sites on <i>lsrACDB</i> side of the <i>lsr</i> operon (at binding sites O3 and O4)	$1 \times 10^{-4} \mu\text{M}$	This paper, assumed
$K_{bind lsrR}$	Michaelis-Menten constant governing the cooperative binding of the <i>lsrR</i> dimer on <i>lsrRK</i> side of <i>lsr</i> operon (at binding sites O1 and O2)	$1 \times 10^{-4} \mu\text{M}$	This paper, assumed
$V_{m lsrA}$	Maximum rate, binding of <i>lsrR</i> dimer to binding sites O3 and O4	$1 \mu\text{M}\cdot\text{min}^{-1}$	This paper, assumed
$V_{m lsrR}$	Maximum rate, binding of <i>lsrR</i> dimer to binding sites O1 and O2	$1 \mu\text{M}\cdot\text{min}^{-1}$	This paper, assumed

k_{bind}	Rate constant governing binding of phospho-AI2 to tetramer, and initial cleavage to two phosphorylated dimers, still bound to the <i>lsr</i> operon	$1 \mu\text{M}^{-2}\text{-min}^{-1}$	This paper, assumed
------------	---	--------------------------------------	---------------------

k_{c1}	Rate constant, governs the binding of cAMP-CRP complex to C1	$1 \mu\text{M}^{-1}\text{-min}^{-1}$	This paper, assumed
k_{c2}	Rate constant, governs the binding of cAMP-CRP complex to C2	$1 \mu\text{M}^{-1}\text{-min}^{-1}$	This paper, assumed
k_{cAMP}	Rate constant governing the binding of cAMP to CRP	$1 \mu\text{M}^{-1}\text{-min}^{-1}$	This paper, assumed
k_{cleave_1}	Rate constant; cleavage of Phospho-AI2/dimer complex from <i>lsrRK</i>	1 min^{-1}	This paper, assumed
k_{cleave_2}	Rate constant; cleavage of Phospho-AI2/dimer complex from <i>lsrACDB</i>	1 min^{-1}	This paper, assumed
k_{deg}	Rate constant; nonspecific protein/nucleoside degradation	1 min^{-1}	This paper, assumed
$k_{\text{deg} Ap}$	Rate constant; specific degradation of phosphor-AI2	1 min^{-1}	This paper, assumed
k_{deg_D}	Rate constant; specific degradation of free <i>lsrR</i> dimer	1 min^{-1}	This paper, assumed
k_{deg_M}	Rate constant; specific degradation of <i>lsrR</i> monomer	1 min^{-1}	This paper, assumed
$k_{\text{deg}_{mRNA}}$	Rate constant;	1 min^{-1}	This paper,

	specific degradation of mRNA		assumed
--	---------------------------------	--	---------

k_{lsrK}	Rate constant; AI-2 phosphorylation by lsrK	1	This paper, assumed
k_{pol}	Rate constant; dimerization of lsrR monomer	$1 \mu\text{M}^{-1}\text{-min}^{-1}$	This paper, assumed
k_{regen}	Rate constant; breakdown of cAMP-CRP complexes bound to lsr operon to cAMP and CRP	$1 \mu\text{M}^{-1}\text{-min}^{-1}$	This paper, assumed

k_{tcA}	Rate constant; maximum transcription rate of mRNA of <i>lsrACDBFG</i> + associated reporter/lacZ	Defined by $B \cdot k_{tcR}$	This paper, defined by model
k_{tcR}	Rate constant; maximum transcription rate of mRNA of <i>lsrRK</i> as defined by our model + associated reporter/lacZ	2.1 min^{-1}	This paper, fitted to Figure 3.6b from [59]
k_{tet}	Rate constant; governing the formation of the lsrR tetramer	$2 \mu\text{M}^{-1} \cdot \text{min}^{-1}$	This paper, assumed
n_A	Cooperativity coefficient; binding of dimer to O3/O4	1.4	This paper, assumed
n_R	Cooperativity coefficient; binding of dimer to O1/O2	1.4	This paper, assumed
α	AI-2 curve fitting parameter; Controls the peak height of the AI-2 curve	$0.005 \mu\text{M}$ (800 Activity Units)	This paper, fitted
β	AI-2 curve fitting parameter; Peak height location; offset from $t = 0$	240 min	[64]

γ	AI-2 curve fitting parameter; Parameter controlling peak width of AI-2 curve	110 min	This paper, fitted
ψ	Conversion factor; molecules/cell to μM concentration	See paper	This paper, converted
κ	Conversion factor to convert from μM concentration to Miller Units (β -galactosidase activity units)	See paper	This paper, converted

References

1. Tunney MM, Dunne N, Einarsson G, McDowell A, Kerr A, et al. (2007) Biofilm formation by bacteria isolated from retrieved failed prosthetic hip implants in an in vitro model of hip arthroplasty antibiotic prophylaxis. *J Orthop Res* 25: 2-10.
2. Soto SM (2013) Role of efflux pumps in the antibiotic resistance of bacteria embedded in a biofilm. *Virulence* 4: 223-229.
3. Zhang L, Mah TF (2008) Involvement of a novel efflux system in biofilm-specific resistance to antibiotics. *J Bacteriol* 190: 4447-4452.
4. Stewart PS, Costerton JW (2001) Antibiotic resistance of bacteria in biofilms. *Lancet* 358: 135-138.
5. Guggenbichler JP, Assadian O, Boeswald M, Kramer A (2011) Incidence and clinical implication of nosocomial infections associated with implantable biomaterials - catheters, ventilator-associated pneumonia, urinary tract infections. *GMS Krankenhhyg Interdiszip* 6: Doc18.
6. Antunes AL, Bonfanti JW, Perez LR, Pinto CC, Freitas AL, et al. (2011) High vancomycin resistance among biofilms produced by *Staphylococcus* species isolated from central venous catheters. *Mem Inst Oswaldo Cruz* 106: 51-55.
7. Wald HL, Kramer AM (2007) Nonpayment for harms resulting from medical care: catheter-associated urinary tract infections. *JAMA* 298: 2782-2784.
8. Santos AP, Watanabe E, Andrade D (2011) Biofilm on artificial pacemaker: fiction or reality? *Arq Bras Cardiol* 97: e113-120.

9. Khardori N, Yassien M (1995) Biofilms in device-related infections. *J Ind Microbiol* 15: 141-147.
10. Janek T, Lukaszewicz M, Krasowska A (2012) Antiadhesive activity of the biosurfactant pseudofactin II secreted by the Arctic bacterium *Pseudomonas fluorescens* BD5. *Bmc Microbiology* 12: 24.
11. Lazar V, Chifiriuc MC (2010) Medical significance and new therapeutical strategies for biofilm associated infections. *Roum Arch Microbiol Immunol* 69: 125-138.
12. Passerini de Rossi B, Feldman L, Pineda MS, Vay C, Franco M (2012) Comparative in vitro efficacies of ethanol-, EDTA- and levofloxacin-based catheter lock solutions on eradication of *Stenotrophomonas maltophilia* biofilms. *J Med Microbiol* 61: 1248-1253.
13. Cobrado L, Silva-Dias A, Azevedo MM, Pina-Vaz C, Rodrigues AG (2013) In vivo antibiofilm effect of cerium, chitosan and hamamelitannin against usual agents of catheter-related bloodstream infections. *J Antimicrob Chemother* 68: 126-130.
14. Kowalczyk D, Ginalska G, Piersiak T, Miazga-Karska M (2012) Prevention of biofilm formation on urinary catheters: comparison of the sparfloxacin-treated long-term antimicrobial catheters with silver-coated ones. *J Biomed Mater Res B Appl Biomater* 100B: 1874-1882.
15. Tenke P, Koves B, Nagy K, Hultgren SJ, Mendling W, et al. (2012) Update on biofilm infections in the urinary tract. *World J Urol* 30: 51-57.

16. Pickard R, Lam T, MacLennan G, Starr K, Kilonzo M, et al. (2012) Antimicrobial catheters for reduction of symptomatic urinary tract infection in adults requiring short-term catheterisation in hospital: a multicentre randomised controlled trial. *Lancet* 380: 1927-1935.
17. Ali JM, Bolton EM, Bradley JA, Pettigrew GJ (2013) Allorecognition pathways in transplant rejection and tolerance. *Transplantation* 96: 681-688.
18. Ibrahim ME, Magzoub MA, Bilal NE, Hamid ME (2013) Distribution of Class I integrons and their effect on the prevalence of multi-drug resistant *Escherichia coli* clinical isolates from Sudan. *Saudi Med J* 34: 240-247.
19. Ibrahim ME, Bilal NE, Hamid ME (2012) Increased multi-drug resistant *Escherichia coli* from hospitals in Khartoum state, Sudan. *Afr Health Sci* 12: 368-375.
20. Lee BY, Yilmaz SL, Wong KF, Bartsch SM, Eubank S, et al. (2013) Modeling the regional spread and control of vancomycin-resistant enterococci. *Am J Infect Control* 41: 668-673.
21. Daneman N, Sarwar S, Fowler RA, Cuthbertson BH (2013) Effect of selective decontamination on antimicrobial resistance in intensive care units: a systematic review and meta-analysis. *Lancet Infect Dis* 13: 328-341.
22. Bodmann KF, Heizmann WR, von Eiff C, Petrik C, Loschmann PA, et al. (2012) Therapy of 1,025 severely ill patients with complicated infections in a German multicenter study: safety profile and efficacy of tigecycline in different treatment modalities. *Chemotherapy* 58: 282-294.

23. Pourakbari B, Aghdam MK, Mahmoudi S, Ashtiani MT, Sabouni F, et al. (2012) High frequency of vancomycin-resistant enterococcus faecalis in an Iranian referral children medical hospital. *Maedica (Buchar)* 7: 201-204.
24. Olawale KO, Fadiora SO, Taiwo SS (2011) Prevalence of hospital-acquired enterococci infections in two primary-care hospitals in osogbo, southwestern Nigeria. *Afr J Infect Dis* 5: 40-46.
25. Christiansen KJ, Turnidge JD, Bell JM, George NM, Pearson JC (2007) Prevalence of antimicrobial resistance in Enterococcus isolates in Australia, 2005: report from the Australian Group on Antimicrobial Resistance. *Commun Dis Intell Q Rep* 31: 392-397.
26. McGoldrick M, Rhinehart E (2007) Managing multidrug-resistant organisms in home care and hospice: surveillance, prevention, and control. *Home Healthc Nurse* 25: 580-586; quiz 587-588.
27. Goossens H (2005) European status of resistance in nosocomial infections. *Chemotherapy* 51: 177-181.
28. Mascini EM, Bonten MJ (2005) Vancomycin-resistant enterococci: consequences for therapy and infection control. *Clin Microbiol Infect* 11 Suppl 4: 43-56.
29. Moran GJ, Abrahamian FM, Lovecchio F, Talan DA (2013) Acute Bacterial Skin Infections: Developments Since the 2005 Infectious Diseases Society of America (IDSA) Guidelines. *J Emerg Med.*

30. Giuffre M, Bonura C, Cipolla D, Mammina C (2013) MRSA infection in the neonatal intensive care unit. *Expert Rev Anti Infect Ther* 11: 499-509.
31. Sherwood J, Park M, Robben P, Whitman T, Ellis MW (2013) USA300 methicillin-resistant *Staphylococcus aureus* emerging as a cause of bloodstream infections at military medical centers. *Infect Control Hosp Epidemiol* 34: 393-399.
32. Jarvis WR, Jarvis AA, Chinn RY (2012) National prevalence of methicillin-resistant *Staphylococcus aureus* in inpatients at United States health care facilities, 2010. *Am J Infect Control* 40: 194-200.
33. Gingrich EN, Kurt T, Hyatt DR, Lappin MR, Ruch-Gallie R (2011) Prevalence of methicillin-resistant staphylococci in northern Colorado shelter animals. *J Vet Diagn Invest* 23: 947-950.
34. Kardas-Sloma L, Boelle PY, Opatowski L, Brun-Buisson C, Guillemot D, et al. (2011) Impact of antibiotic exposure patterns on selection of community-associated methicillin-resistant *Staphylococcus aureus* in hospital settings. *Antimicrob Agents Chemother* 55: 4888-4895.
35. Mera RM, Suaya JA, Amrine-Madsen H, Hoge CS, Miller LA, et al. (2011) Increasing role of *Staphylococcus aureus* and community-acquired methicillin-resistant *Staphylococcus aureus* infections in the United States: a 10-year trend of replacement and expansion. *Microb Drug Resist* 17: 321-328.

36. Lin Y, Barker E, Kislow J, Kaldhone P, Stemper ME, et al. (2011) Evidence of multiple virulence subtypes in nosocomial and community-associated MRSA genotypes in companion animals from the upper midwestern and northeastern United States. *Clin Med Res* 9: 7-16.
37. Huang SS, Yokoe DS, Stelling J, Placzek H, Kulldorff M, et al. (2010) Automated detection of infectious disease outbreaks in hospitals: a retrospective cohort study. *PLoS Med* 7: e1000238.
38. Bordon J, Master RN, Clark RB, Duvvuri P, Karlowsky JA, et al. (2010) Methicillin-resistant *Staphylococcus aureus* resistance to non-beta-lactam antimicrobials in the United States from 1996 to 2008. *Diagn Microbiol Infect Dis* 67: 395-398.
39. Boneca IG, Chiosis G (2003) Vancomycin resistance: occurrence, mechanisms and strategies to combat it. *Expert Opin Ther Targets* 7: 311-328.
40. Wood KB, Cluzel P (2012) Trade-offs between drug toxicity and benefit in the multi-antibiotic resistance system underlie optimal growth of *E. coli*. *BMC Syst Biol* 6: 48.
41. Martins M, McCusker MP, Viveiros M, Couto I, Fanning S, et al. (2013) A Simple Method for Assessment of MDR Bacteria for Over-Expressed Efflux Pumps. *Open Microbiol J* 7: 72-82.
42. Baugh S, Ekanayaka AS, Piddock LJ, Webber MA (2012) Loss of or inhibition of all multidrug resistance efflux pumps of *Salmonella enterica* serovar Typhimurium results in impaired ability to form a biofilm. *J Antimicrob Chemother* 67: 2409-2417.

43. Hooshangi S, Bentley WE (2011) LsrR quorum sensing "switch" is revealed by a bottom-up approach. *PLoS Comput Biol* 7: e1002172.
44. Roy V, Smith JA, Wang J, Stewart JE, Bentley WE, et al. (2010) Synthetic analogs tailor native AI-2 signaling across bacterial species. *J Am Chem Soc* 132: 11141-11150.
45. Roy V, Fernandes R, Tsao CY, Bentley WE (2010) Cross species quorum quenching using a native AI-2 processing enzyme. *ACS Chem Biol* 5: 223-232.
46. Taga ME, Semmelhack JL, Bassler BL (2001) The LuxS-dependent autoinducer AI-2 controls the expression of an ABC transporter that functions in AI-2 uptake in *Salmonella typhimurium*. *Mol Microbiol* 42: 777-793.
47. Surette MG, Miller MB, Bassler BL (1999) Quorum sensing in *Escherichia coli*, *Salmonella typhimurium*, and *Vibrio harveyi*: a new family of genes responsible for autoinducer production. *Proc Natl Acad Sci U S A* 96: 1639-1644.
48. Bassler BL (1999) How bacteria talk to each other: regulation of gene expression by quorum sensing. *Curr Opin Microbiol* 2: 582-587.
49. Bassler BL, Greenberg EP, Stevens AM (1997) Cross-species induction of luminescence in the quorum-sensing bacterium *Vibrio harveyi*. *J Bacteriol* 179: 4043-4045.
50. Zhu C, Feng S, Sperandio V, Yang Z, Thate TE, et al. (2007) The possible influence of LuxS in the in vivo virulence of rabbit enteropathogenic *Escherichia coli*. *Vet Microbiol* 125: 313-322.

51. Kendall MM, Rasko DA, Sperandio V (2007) Global effects of the cell-to-cell signaling molecules autoinducer-2, autoinducer-3, and epinephrine in a luxS mutant of enterohemorrhagic Escherichia coli. *Infect Immun* 75: 4875-4884.
52. Sperandio V, Torres AG, Kaper JB (2002) Quorum sensing Escherichia coli regulators B and C (QseBC): a novel two-component regulatory system involved in the regulation of flagella and motility by quorum sensing in E. coli. *Mol Microbiol* 43: 809-821.
53. Hardie KR, Heurlier K (2008) Establishing bacterial communities by 'word of mouth': LuxS and autoinducer 2 in biofilm development. *Nature Reviews Microbiology* 6: 635-643.
54. Hegde M, Englert DL, Schrock S, Cohn WB, Vogt C, et al. (2011) Chemotaxis to the quorum-sensing signal AI-2 requires the Tsr chemoreceptor and the periplasmic LsrB AI-2-binding protein. *J Bacteriol* 193: 768-773.
55. Quan DN, Bentley WE (2012) Gene network homology in prokaryotes using a similarity search approach: queries of quorum sensing signal transduction. *PLoS Comput Biol* 8: e1002637.
56. Roy V, Adams BL, Bentley WE (2011) Developing next generation antimicrobials by intercepting AI-2 mediated quorum sensing. *Enzyme Microb Technol* 49: 113-123.
57. Tsao CY, Hooshangi S, Wu HC, Valdes JJ, Bentley WE (2010) Autonomous induction of recombinant proteins by minimally rewiring native quorum sensing regulon of E. coli. *Metab Eng* 12: 291-297.

58. Hooshangi S, Bentley WE (2008) From unicellular properties to multicellular behavior: bacteria quorum sensing circuitry and applications. *Curr Opin Biotechnol* 19: 550-555.
59. Byrd CM (2011) LOCAL AND GLOBAL GENE REGULATION ANALYSIS OF THE AUTOINDUCER-2 MEDIATED QUORUM SENSING MECHANISM IN *ESCHERICHIA COLI*: University of Maryland at College Park.
60. Roy V, Meyer MT, Smith JA, Gamby S, Sintim HO, et al. (2013) AI-2 analogs and antibiotics: a synergistic approach to reduce bacterial biofilms. *Appl Microbiol Biotechnol* 97: 2627-2638.
61. Jiang T, Li M (2013) Quorum sensing inhibitors: a patent review. *Expert Opin Ther Pat.*
62. Varga ZG, Armada A, Cerca P, Amaral L, Mior Ahmad Subki MA, et al. (2012) Inhibition of quorum sensing and efflux pump system by trifluoromethyl ketone proton pump inhibitors. *In Vivo* 26: 277-285.
63. Wang L, Li J, March JC, Valdes JJ, Bentley WE (2005) luxS-dependent gene regulation in *Escherichia coli* K-12 revealed by genomic expression profiling. *J Bacteriol* 187: 8350-8360.
64. Wang L, Hashimoto Y, Tsao CY, Valdes JJ, Bentley WE (2005) Cyclic AMP (cAMP) and cAMP receptor protein influence both synthesis and uptake of extracellular autoinducer 2 in *Escherichia coli*. *J Bacteriol* 187: 2066-2076.

65. Veselova MA, Lipasova VA, Zaitseva Iu V, Koksharova OA, Chernukha M, et al. (2012) [Mutants of *Burkholderia cenocepacia* with a change in synthesis of N-acyl-homoserine lactones--signal molecules of Quorum Sensing regulation]. *Genetika* 48: 608-616.
66. Pereira CS, Santos AJ, Bejerano-Sagie M, Correia PB, Marques JC, et al. (2012) Phosphoenolpyruvate phosphotransferase system regulates detection and processing of the quorum sensing signal autoinducer-2. *Mol Microbiol* 84: 93-104.
67. Lengeler JW, Jahreis K (2009) Bacterial PEP-dependent carbohydrate: phosphotransferase systems couple sensing and global control mechanisms. *Contrib Microbiol* 16: 65-87.
68. Herzberg M, Kaye IK, Peti W, Wood TK (2006) YdgG (TqsA) controls biofilm formation in *Escherichia coli* K-12 through autoinducer 2 transport. *J Bacteriol* 188: 587-598.
69. Luo X, Wu HC, Tsao CY, Cheng Y, Betz J, et al. (2012) Biofabrication of stratified biofilm mimics for observation and control of bacterial signaling. *Biomaterials* 33: 5136-5143.
70. Xavier KB, Miller ST, Lu W, Kim JH, Rabinowitz J, et al. (2007) Phosphorylation and processing of the quorum-sensing molecule autoinducer-2 in enteric bacteria. *ACS Chem Biol* 2: 128-136.
71. Taga ME, Miller ST, Bassler BL (2003) Lsr-mediated transport and processing of AI-2 in *Salmonella typhimurium*. *Mol Microbiol* 50: 1411-1427.

72. Marques JC, Lamosa P, Russell C, Ventura R, Maycock C, et al. (2011) Processing the interspecies quorum-sensing signal autoinducer-2 (AI-2): characterization of phospho-(S)-4,5-dihydroxy-2,3-pentanedione isomerization by LsrG protein. *J Biol Chem* 286: 18331-18343.
73. Liu X, Wu M, Sun D, Zang J (2010) Cloning, purification, crystallization and preliminary crystallographic analysis of LsrR from *Escherichia coli*. *Acta Crystallogr Sect F Struct Biol Cryst Commun* 66: 913-915.
74. Blazy B, Takahashi M, Baudras A (1980) Binding of CRP to DNA-dependent RNA polymerase from *E. coli*: modulation by cAMP of the interactions with free and DNA-bound holo and core enzyme. *Mol Biol Rep* 6: 39-43.
75. Wong P, Gladney S, Keasling JD (1997) Mathematical model of the lac operon: Inducer exclusion, catabolite repression, and diauxic growth on glucose and lactose. *Biotechnol Prog* 13: 132-143.
76. Byrd C, Servinsky MD, Bentley WE (In Preparation) Transcriptional Regulation in the Divergent Quorum Sensing *lsr* Regulon in *Escherichia coli*. *J Bacteriol*.
77. Wu M, Tao Y, Liu X, Zang J (2013) Structural basis for phosphorylated autoinducer-2 modulation of the oligomerization state of the global transcription regulator LsrR from *Escherichia coli*. *J Biol Chem*.
78. Xavier KB, Bassler BL (2005) Regulation of uptake and processing of the quorum-sensing autoinducer AI-2 in *Escherichia coli*. *J Bacteriol* 187: 238-248.

79. Li J, Wang L, Hashimoto Y, Tsao CY, Wood TK, et al. (2006) A stochastic model of Escherichia coli AI-2 quorum signal circuit reveals alternative synthesis pathways. *Molecular Systems Biology* 2: 67.
80. Li J, Attila C, Wang L, Wood TK, Valdes JJ, et al. (2007) Quorum sensing in Escherichia coli is signaled by AI-2/LsrR: effects on small RNA and biofilm architecture. *J Bacteriol* 189: 6011-6020.
81. Trappetti C, Potter AJ, Paton AW, Oggioni MR, Paton JC (2011) LuxS mediates iron-dependent biofilm formation, competence, and fratricide in *Streptococcus pneumoniae*. *Infect Immun* 79: 4550-4558.
82. Gonzalez Barrios AF, Achenie LE (2010) Escherichia coli autoinducer-2 uptake network does not display hysteretic behavior but AI-2 synthesis rate controls transient bifurcation. *Biosystems* 99: 17-26.
83. Zorrilla S, Doan T, Alfonso C, Margeat E, Ortega A, et al. (2007) Inducer-modulated cooperative binding of the tetrameric CggR repressor to operator DNA. *Biophysical Journal* 92: 3215–3227.
84. Pitre CA, Tanner JR, Patel P, Brassinga AK (2013) Regulatory control of temporally expressed integration host factor (IHF) in *Legionella pneumophila*. *Microbiology* 159: 475-492.
85. Yona-Nadler C, Umanski T, Aizawa S, Friedberg D, Rosenshine I (2003) Integration host factor (IHF) mediates repression of flagella in enteropathogenic and enterohaemorrhagic Escherichia coli. *Microbiology* 149: 877-884.

86. Spira B, Yagil E (1999) The integration host factor (IHF) affects the expression of the phosphate-binding protein and of alkaline phosphatase in *Escherichia coli*. *Current Microbiology* 38: 80-85.
87. Vivas P, Velmurugu Y, Kuznetsov SV, Rice PA, Ansari A (2013) Global analysis of ion dependence unveils hidden steps in DNA binding and bending by integration host factor. *The Journal of Chemical Physics* 139: 121927.
88. Mangan MW, Lucchini S, Danino V, Croinin TO, Hinton JC, et al. (2006) The integration host factor (IHF) integrates stationary-phase and virulence gene expression in *Salmonella enterica* serovar Typhimurium. *Mol Microbiol* 59: 1831-1847.
89. Sarkar T, Petrov AS, Vitko JR, Santai CT, Harvey SC, et al. (2009) Integration host factor (IHF) dictates the structure of polyamine-DNA condensates: implications for the role of IHF in the compaction of bacterial chromatin. *Biochemistry* 48: 667-675.
90. Ali BM, Amit R, Braslavsky I, Oppenheim AB, Gileadi O, et al. (2001) Compaction of single DNA molecules induced by binding of integration host factor (IHF). *Proc Natl Acad Sci U S A* 98: 10658-10663.
91. Filutowicz M, Inman R (1991) A compact nucleoprotein structure is produced by binding of *Escherichia coli* integration host factor (IHF) to the replication origin of plasmid R6K. *J Biol Chem* 266: 24077-24083.

92. Choi J, Shin D, Kim M, Park J, Lim S, et al. (2012) LsrR-mediated quorum sensing controls invasiveness of *Salmonella typhimurium* by regulating SPI-1 and flagella genes. *PLoS One* 7: e37059.
93. Kalia VC, Wood TK, Kumar P (2013) Evolution of Resistance to Quorum-Sensing Inhibitors. *Microbial Ecology*: 1-12.
94. Torres-Escobar A, Juarez-Rodriguez MD, Lamont RJ, Demuth DR (2013) Transcriptional regulation of *Aggregatibacter actinomycetemcomitans* lsrACDBFG and lsrRK operons and their role in biofilm formation. *J Bacteriol* 195: 56-65.
95. Azakami H, Teramura I, Matsunaga T, Akimichi H, Noiri Y, et al. (2006) Characterization of autoinducer 2 signal in *Eikenella corrodens* and its role in biofilm formation. *J Biosci Bioeng* 102: 110-117.
96. Balestrino D, Haagensen JA, Rich C, Forestier C (2005) Characterization of type 2 quorum sensing in *Klebsiella pneumoniae* and relationship with biofilm formation. *J Bacteriol* 187: 2870-2880.
97. Challan Belval S, Gal L, Margiewes S, Garmyn D, Piveteau P, et al. (2006) Assessment of the roles of LuxS, S-ribosyl homocysteine, and autoinducer 2 in cell attachment during biofilm formation by *Listeria monocytogenes* EGD-e. *Appl Environ Microbiol* 72: 2644-2650.
98. De Keersmaecker SC, Varszegi C, van Boxel N, Habel LW, Metzger K, et al. (2005) Chemical synthesis of (S)-4,5-dihydroxy-2,3-pentanedione, a bacterial signal molecule precursor, and validation of its activity in *Salmonella typhimurium*. *J Biol Chem* 280: 19563-19568.

99. Fernandes R, Bentley WE (2009) AI-2 biosynthesis module in a magnetic nanofactory alters bacterial response via localized synthesis and delivery. *Biotechnol Bioeng* 102: 390-399.
100. Wei JR, Lai HC (2006) N-acylhomoserine lactone-dependent cell-to-cell communication and social behavior in the genus *Serratia*. *Int J Med Microbiol* 296: 117-124.
101. Zhu J, Hixon MS, Globisch D, Kaufmann GF, Janda KD (2013) Mechanistic Insights into the LsrK Kinase Required for Autoinducer-2 Quorum Sensing Activation. *Journal of the American Chemical Society* 135: 7827-7830.
102. Ha J-H, Eo Y, Grishaev A, Guo M, Smith JAI, et al. (2013) Crystal Structures of the LsrR Proteins Complexed with Phospho-AI-2 and Two Signal-Interrupting Analogues Reveal Distinct Mechanisms for Ligand Recognition. *Journal of the American Chemical Society* ARTICLE ASAP.
103. Kleina LG, Miller JH (1990) Genetic studies of the lac repressor. XIII. Extensive amino acid replacements generated by the use of natural and synthetic nonsense suppressors. *J Mol Biol* 212: 295-318.
104. Jarema MA, Lu P, Miller JH (1980) Lac repressor: a genetic and nuclear magnetic resonance study of structure and function. *Biophys J* 32: 450-452.
105. Miller JH (1980) Genetic analysis of the lac repressor. *Curr Top Microbiol Immunol* 90: 1-18.

106. Lee SB, Bailey JE (1984) Genetically Structured Models for Iac Promoter-Operator Function in the Chromosome and in Multicopy Plasmids - Iac Promoter Function. *Biotechnol Bioeng* 26: 1383-1389.
107. Lee SB, Bailey JE (1984) Genetically structured models for lac promoter-operator function in the chromosome and in multicopy plasmids: Lac promoter function. *Biotechnol Bioeng* 26: 1383-1389.

